Review article

Sajid M. Choudhury, Di Wang, Krishnakali Chaudhuri, Clayton DeVault, Alexander V. Kildishev, Alexandra Boltasseva and Vladimir M. Shalaev*

Material platforms for optical metasurfaces

https://doi.org/10.1515/nanoph-2017-0130
Received December 20, 2017; revised March 6, 2018; accepted March 22, 2018

Abstract: Optical metasurfaces are judicously engineered electromagnetic interfaces that can control and manipulate many of light's quintessential properties, such as amplitude, phase, and polarization. These artificial surfaces are composed of subwavelength arrays of optical antennas that experience resonant light-matter interaction with incoming electromagnetic radiation. Their ability to arbitrarily engineer optical interactions has generated considerable excitement and interest in recent years and is a promising methodology for miniaturizing optical components for applications in optical communication systems, imaging, sensing, and optical manipulation. However, development of optical metasurfaces requires progress and solutions to inherent challenges, namely large losses often associated with the resonant structures; large-scale, complementary metal-oxide-semiconductor-compatible nanofabrication techniques; and incorporation of active control elements. Furthermore, practical metasurface devices require robust operation in high-temperature environments, caustic chemicals, and intense electromagnetic fields. Although these challenges are substantial, optical metasurfaces remain in their infancy, and novel material platforms that offer resilient, low-loss, and tunable metasurface designs are driving new and promising routes for overcoming these hurdles. In this review, we discuss the different material platforms in the literature for various applications of metasurfaces, including refractory plasmonic materials, epitaxial noble metal, silicon, graphene, phase change materials, and metal oxides. We identify the key advantages of each material platform and review the breakthrough devices that were made possible with each material. Finally, we provide an outlook for emerging metasurface devices and the new material platforms that are enabling such devices.

Keywords: materials platforms; metasurface; plasmonics; dielectric metasurface.

***Corresponding author: Vladimir M. Shalaev,** School of Electrical and Computer Engineering and Birck Nanotechnology Center, Purdue University, 1205 W State St. West Lafayette, IN 47907, USA, e-mail: shalaev@purdue.edu
Sajid M. Choudhury, Di Wang, Krishnakali Chaudhuri, Alexander V. Kildishev and Alexandra Boltasseva: School of Electrical and Computer Engineering and Birck Nanotechnology Center, Purdue University, West Lafayette, IN 47907, USA
Clayton DeVault: Department of Physics and Birck Nanotechnology Center, Purdue University, West Lafayette, IN 47907, USA

1 Introduction

Harnessing, controlling, and understanding light have been long-standing pursuits of human civilization, dating back to ancient times. After years of exploration and discovery, we find ourselves now surrounded with optical technologies that have advanced our ability to detect early signs of disease, transmit data across the world at the speed of light, and stream high-definition movies on our phones during class lectures. Optics has revolutionized the world – yet, after so much progress and discovery, most of our modern devices still resemble and rely on basic and bulky optical components such as lenses, mirrors, and prisms for steering light. With current trends to progressively miniaturize technology, it is now essential to look for alternative methods to control light at extremely small dimensions. This miniaturization requires compact and planar devices with novel functionalities that can now be realized via novel approaches that utilize artificial composite optical materials. Metamaterials (MMs) are artificial materials composed of periodic or specially arranged metal/dielectric structural elements with deeply subwavelength dimensions. Engineered MMs exhibit artificial optical properties that are very different from the properties of their constituent materials. The electromagnetic properties of MMs can be tailored and manipulated almost at will via smart design techniques, making MMs a promising platform to overcome many of the limitations of conventional optical elements. MMs can couple to the electric and magnetic fields of incident light and demonstrate effective properties for electric (permittivity) and magnetic (permeability) field interactions that are not usually found in nature. Such materials can

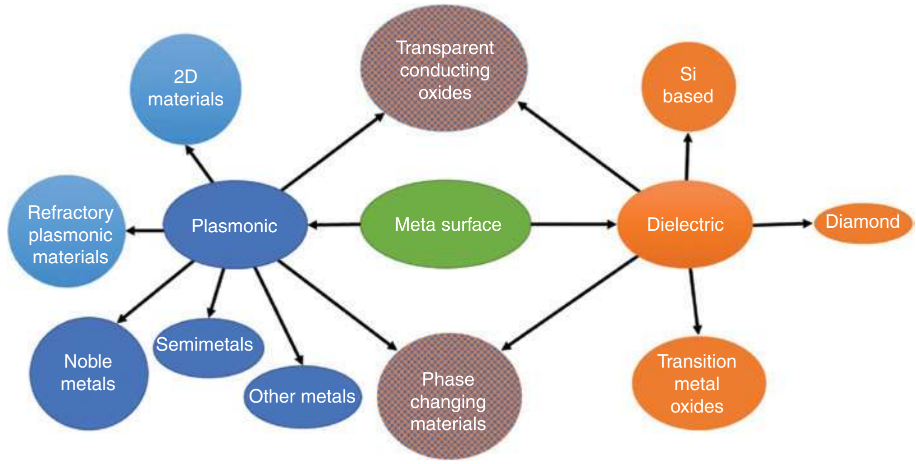

Figure 1: Conventional and emerging material platforms for optical metasurfaces including noble and other commonly used in plasmonics metals; semimetals and intermetallic compounds exhibiting metallic behavior (such as metal nitrides, hydrides, oxides, borides, etc.); transparent conducting oxides; and dielectrics.

realize effective negative refractive index [1] and thereby can be utilized to make new devices such as lenses that can image beyond the diffraction limit [2] or invisibility cloaks [3]. Practical realization of such MMs is limited due to numerous challenges such as harsh microfabrication and nanofabrication requirement for layered structures and significant optical losses in the materials.

Optical metasurfaces that represent a special class of two-dimensional (2D) MMs can overcome the size limitations of both conventional optical elements as well as fabrication challenges of bulk 3D MMs. A metasurface manipulates light using a 2D array of optical scatterers with a subwavelength distance between the scatterers. These scatterers themselves are smaller than the wavelength scale, and the metasurfaces can modulate incoming light in both amplitude and phase having their total thickness much smaller than the wavelength. The scatterers can be either metallic or dielectric structured nanoparticles or subwavelength apertures in a metallic or dielectric thin film. While for phase control, a conventional optical element relies on continuous phase accumulation through light propagation, the optical scatterers in a metasurface can introduce an abrupt phase change to the electromagnetic waves that they interact with.

There are numerous review articles related to the development and seminal works of metasurfaces as well as applications and metasurfaces for specific material platforms [4–15]. For our review, we focus on the different material platforms of metasurfaces, shown in Figure 1. In a broad context, all metasurfaces can be divided into two general classes – plasmonic and dielectric metasurfaces, which are discussed in Sections 2 and 3, respectively. Section 4 describes the emerging material platforms for metasurfaces, namely new materials for specialized applications such as transition metal nitrides, transparent conducting oxides, high-K dielectrics, and tunable materials such as Ga:ZnO and ultra-low footprint materials such as graphene. Finally, Section 5 discusses emerging applications and potential future developments for metasurfaces and how the materials play a role in it.

In this review, we primarily emphasize on the emerging material platforms of metasurface beyond noble metals and high-index dielectric studied before and compare them with the traditional material platforms, identifying the key advantages and limitations of each. Table 1 gives a general overview of the material classes that are described in detail throughout the article.

2 Plasmonic metasurfaces

Tiny nanoparticles of noble metals have been used to color glass since ancient times [16]. A fourth century Roman Lycurgus cup shows different colors when the light is shone through it and when the light is reflected off from it. Polychrome luster decorations from the Abbasid era [17] and Cassius purple and ruby glass from the renaissance period [18] demonstrate colorful pottery by using the characteristic red color of spherical gold nanoparticles. Such coloration can be explained by the interaction between nanoparticles and light, which forms the fundamental principle of plasmonics and plasmonic metasurfaces. Plasmonics deals with the coupling between the electromagnetic field and the electronic oscillations of material. Plasmon is a quantum of free electron oscillation.

Table 1: Different material platforms with their wavelength range, advantages, limitations and applications.

Material type	Examples	Wavelength range	Advantages	Limitations/challenges	Application examples
Plasmonic metal	Au, Ag, Al, Cu…	Visible–mid IR	Established fabrication Plasmonic in the UV part of the spectrum (Ag, Al) Biocompatible (Au) Small device footprint High field concentration	Relatively low melting point; Lack of tunability High solubility/diffusion at elevated temperature Low chemical stability (Ag, Al)	Proof-of-concept demonstrations of compact and flat optical devices Biosensing (Au) Structured coloration and holography (Al)
Refractory	TiN, ZrN, HfN, W, Ta…	Visible–mid IR	High durability High melting point CMOS compatible Chemical stability (TiN) Biocompatible (TiN) Low solubility Epitaxially grown Possibility of growing ultra-thin films (few nm)	Higher optical loss in visible compared to noble metals Strict fabrication requirements	Local heating and absorbers High temperature and high intensities Fabrication of epitaxial Ag (TiN) Biomedical thermo-plasmonics (TiN)
2D	Graphene, MXene, phorsphorene, MoS_2, WSe_2, WS_2…	Near–Mid IR	Dynamic tunability (electrical) Fast modulation Large field confinement Compactness/lightweight Mechanical flexibility Lower loss than noble metals in near IR	Poor light absorption with single layer	Dynamically tunable and flexible devices
Phase change	GST, VO_2, YH_2, MgH_2, PdH_2, $SmNiO_3$	Near–mid IR	Dynamic tunability (temperature) Large optical modulation	Relatively slow modulation	Nonvolatile reversible optical switches
Transparent conducting oxides	ITO, Ga:ZnO, Al:ZnO	Near–mid IR	ENZ in near IR Ultrafast tunability (optical, electrical, temperature)	Less plasmonic in the NIR compared to noble metals	Ultrafast optical modulators
Dielectric	Si, TiO_2, SiO_2, Si_3N_4, diamond	Visible–near IR	Very low optical loss Mechanical and chemical robustness	Larger device footprint Low field confinement	Highly efficient metasurfaces

Free electron clouds in a metal can couple to light at an interface between metal and dielectric media and create surface plasmons. With adequately designed nanostructures made from metals, the surface plasmons make it possible to control light at the subdiffraction scale.

Not only can the plasmonic nanostructures guide light at the nanoscale, but they can also increase the local intensity of an electromagnetic field by orders of magnitude. This enhancement is possible due to the strong local field confinement near the metal surface of a nanostructure. For metallic subwavelength structures or nanoparticles, the electric field of incoming radiation can polarize the conduction electrons. The resulting plasmon oscillations are distributed over the nanoparticle volume and are localized within the particle. These plasmon oscillations are termed localized surface plasmons (LSPs). The displacement of the electron clouds from the lattice generates a restoring force that tries to pull the electrons back into the lattice. The nanoparticle therefore acts as an oscillator driven by the incoming field together with restoring Coulomb force and behaves as a simple dipole in the direction of the electric field. When the frequency matches the resonance-frequency defined by the shape of the particle, LSP resonance occurs, enhancing local field amplitude. The nanostructures can also introduce a local phase shift to the incoming light beam and manipulate its wavefront.

The concept of local phase shift generation using plasmonic nanostructures can be employed by introducing abrupt phase jumps with metasurfaces. When light travels through a plane that can introduce abrupt phase change, it has been shown that the light propagation needs to be explained with a modification of Snell's law by introducing an artificially engineered phase-gradient term. The resulting phase-gradient from a subwavelength thick structure is shown to bend light in anomalous directions [19]. Since most of the conventional optical devices rely on amplitude or phase modulation of the incoming light, the ability of plasmonic nanostructures to introduce the abrupt phase shift can be used to engineer ultracompact optical devices. An early demonstration of the photonic spin Hall effect (PSHE), with polarization-dependent splitting of light, is also achieved by plasmonic metasurface [20]. Seminal work on plasmonic antennas with aluminum [21] spearheaded the field of Al-based plasmonic metasurfaces. Many of the first applications of metasurfaces demonstrate imaging and sensing at the nanoscale, namely subdiffraction lensing [22–27], spectroscopy [28], monochromatic holography [29–36], color holography [37–40], polarization converters [41–46], vortex plates [47–49], invisibility cloaks [50], polarization-selective elements [51–54], etc.

Despite all the promising applications of plasmonic metasurfaces, optical losses in plasmonic devices severely limit their use in replacing conventional optical elements. As electron clouds in the metal oscillate while interacting with the incoming electromagnetic wave, they experience scattering in the material that causes heat generation. Although, for the best plasmonic material, low loss (small imaginary part of permittivity) and high plasmonic property (large negative real part of permittivity) are essential, the losses cannot be avoided entirely. Even for an ideal plasmonic material with negligible loss, nanostructuring the metal causes the magnetic field of an incoming electromagnetic wave to be truncated as the wave interacts with the free electrons of the structure. Truncating the magnetic field, in turn, results in the conversion of stored magnetic energy into kinetic energy of electrons and causes a loss termed the Landau damping [55]. Compared to dielectric metasurfaces, discussed in the next section, plasmonic metasurfaces will be therefore inherently less efficient but will have tighter field confinement, broader bandwidth, and smaller device footprint. For applications specific to plasmonic metasurface, the tradeoff between field confinement and loss must be made. Plasmonic metasurfaces are particularly useful, however, when optical losses are desired, such as in heating or absorber devices. Scattering loss minimization for plasmonic metasurface has been proposed through impedance matching [56], but the rest of the losses are inherent in plasmonic systems. Applications for plasmonic metasurfaces are emerging, exploiting their ability to strongly confine field such as color filter and displays [57–59], enhanced harmonic generation [60–62], improved nonlinearity [63, 64], detection sensitivity improvement [65–67], absorbers [68–70], perfect absorber and efficient thermal emitters [71–73], photocatalysis [74], high-temperature applications such as thermo-photovoltaics [75], heat-assisted magnetic recording (HAMR) [76], etc.

Conventional plasmonic materials such as gold and silver have been historically used for most of the early metasurface applications. Bulk silver has good plasmonic properties in the visible frequencies, but evaporated silver, which is most commonly used in metasurfaces due to the relatively easy fabrication, is prone to be lossier due to electron scattering at grain boundaries. Also, it is fundamentally challenging to grow ultrathin (on the order of few nanometers) gold and silver films because these two materials tend to form nanoislands rather than continuous films at thicknesses below 10 nm. From the fabrication standpoint, gold and silver are also not compatible with the standard complementary metal-oxide-semiconductor (CMOS) technology, as silver has low chemical stability and gold is easily diffused into the substrate. Additionally, these noble metals have low melting temperatures. Therefore, the nanostructures made of noble metals easily deform at elevated temperatures. Consequently, noble metals are not suitable for high-temperature applications, which is a dilemma for plasmonics because the plasmon oscillations unavoidably heat up the metals significantly, at least within the spatial field confinement. Recently, it has been shown that thin dielectric coated nanostructured metal can be used for refractory plasmonics and nonlinear optics applications, by improving the temperature stability of the structured metal [77, 78]. For stronger field confinement and high-temperature applications beyond noble metals' capabilities, new plasmonic materials are necessary. The study of alternative plasmonic materials has become a new field of itself and has found functional devices using the merger of metasurface with these materials' applications [79].

In the paper, we discuss in more detail the refractory plasmonic materials and 2D materials as platforms for plasmonic materials and discuss epitaxially grown noble metals with the help of alternative plasmonic materials. We did not discuss many other alternative plasmonic materials that have no demonstrated metasurface application or applications are very limited due to fabrication challenge or poor plasmonic properties. For a detailed review of plasmonic materials, please refer to the review by Naik et al. [80].

3 Dielectric metasurfaces

Since the onset of the successful demonstration of light bending at ultrathin scale [19, 81], the field of plasmonic metasurface has seen rapid growth due to the compactness, high optical confinement, and efficient hot electron generation found in such systems. As discussed in the previous section, plasmonic metasurfaces suffer from intrinsic optical losses because of strong electron-electron and electron-phonon scattering in metals, which limit the efficiency of functional optical devices such as lenses, holograms, wave plates, spectrometers, etc. [55]. The quest for highly efficient planar optical manipulators has led to the development of all-dielectric metasurfaces. Unlike plasmonic metasurfaces, which rely on LSP resonances to realize their features, dielectric metasurfaces are based on the collective light scattering (known as Mie scattering) off the constituent high-index dielectric nanoparticles with dimensions comparable to the wavelength of light inside the particles [82–85].

Optical loss can be minimized in all-dielectric metasurfaces as the large bandgap energies in dielectric materials limit optically induced interband transitions. Therefore, when light (with sub-bandgap energies) impinges upon dielectric nanoparticles, no free charge carriers are available, and only displacement currents instead of conduction currents are induced. This results in negligible optical losses and high electric field concentration inside the dielectric nanoparticles, in contrast to metallic nanoparticles where a significant portion of the incident optical energy converts to heat and strong electric field concentration happens close to the surface outside the nanoparticles. Because of the low-loss feature, all-dielectric metasurfaces significantly surpass plasmonic metasurfaces in efficiency and resonance quality factor. Electromagnetically induced transparency (EIT) with a quality factor of ~600 has been demonstrated in all-dielectric metasurfaces [86, 87], representing an enormous advancement from plasmonic EIT metasurfaces with a quality factor on the order of 10. It has been recently pointed out that bounded states in the continuum can be excited in all-dielectric metasurfaces with even higher quality factors (in theory, infinite quality factor for metasurfaces with infinitely large lateral dimensions) [88], efforts toward this direction are underway among several research groups. While it might not be surprising that all-dielectric metasurfaces outperform metallic metasurfaces in transmission applications since metals exhibit large optical reflection and absorption, even in reflectors where metals find most efficient applications, experimentally demonstrated all-dielectric near-perfect (99.7%) reflectors outperform metallic mirrors in efficiency which experience ~2% intrinsic loss [89, 90].

The optically induced magnetic response in metallic nanoparticles (other than split-ring structures) is negligible because the field vanishes inside the particle. In dielectric nanoparticles, however, both electric and magnetic responses of similar strengths can be observed. Strong magnetic dipole resonance arises in dielectric nanoparticles when the induced displacement current circulates inside the nanoparticle, and electric dipole resonance arises when induced displacement current oscillates linearly. The possibility to engineer both electric and magnetic resonances in dielectric nanoparticles endows all-dielectric metasurfaces with functionalities unattainable in their plasmonic counterparts. First, dielectric nanoparticles can be engineered for unidirectional light scattering. For dielectric nanoparticles of a certain size, at some well-defined frequency, the electric and magnetic dipoles can be excited to oscillate in phase with equal strengths. Under such condition, the Mie theory shows that the backscattering cross-section diminishes due to the destructive inference from the two dipole oscillations [82, 91]. This principle has been used to engineer flat reflection-less all dielectric metasurfaces, manifesting itself as an advantage over conventional optics, as multiple optical layers or components are usually required to eliminate the back reflection. Second, the near-field enhancement of dielectric nanoparticles can be utilized to enhance nonlinear effects. In a recent work, Shcherbakov et al. [92] showed that the third harmonic generation (THG) intensity could be improved by two orders of magnitude in silicon nanodisks compared to unstructured bulk silicon close to the magnetic dipole resonance. THG enhancement has also been demonstrated with silicon metasurface exhibiting strong near-field enhancement from Fano-type resonance by Yang et al. [93] who achieved a THG enhancement factor of 1.5×10^5 on Si metasurface relative to unpatterned silicon. Similar studies on nonlinear effects can be potentially carried out on metasurfaces made of diamond, a material that exhibits relatively high refractive index and can handle high optical powers [94]. Additionally, with the recent progress toward integrated diamond photonics and color centers [95–100], diamond metalens has been made to image single quantum emitters *in situ* [101].

In addition to unidirectional scattering and nonlinear effect enhancement, engineering of both electric and magnetic resonances in dielectric nanoparticles also enables redirecting light with more control than plasmonic metasurfaces. Similar to plasmonic metasurfaces, light manipulation (focusing, diffraction, beam steering, holography, etc.) with dielectric metasurfaces is achieved via phase control by individual subwavelength optical scatterers or pixels. Early in the 1990s, a very similar technique has been developed based on mimicking gradient index material with pixelated dielectric pillars whose local effective index is controlled by the filling ratio of dielectric to air in each pixel [102–104]. As the research field developed, the technique shifted to controlling the phase of the scattered light by varying the dimensions (and sometimes the shape) of dielectric scatterers, so that the scattered light from individual scatterers interfere and form a desired wavefront in the far field. The presence of both electric and magnetic resonances in the same frequency range enables full 2π phase control in a single dielectric structure layer by varying only the size of the dielectric nanoparticle, whereas only π phase control can be achieved using single layer plasmonic structures. Because the phase tuning happens close to the electric and magnetic dipole resonances, such phase control technique is named resonant tuning [105–110]. The scattered light from resonant tuning metasurfaces has the same polarization as the incident light. Phase control with dielectric metasurface can also be achieved in a nonresonant manner, which requires birefringent elements, hence is termed geometric tuning [111–115]. The birefringent element imparts phase shifts ϕ_x and ϕ_y on light linearly polarized along its fast and slow axes. For half-wave plate birefringent elements ($|\phi_x - \phi_y| = \pi$), the imparted phase profile is equal to $\phi(x, y) = 2\theta(x, y)$, where $\theta(x, y)$ is the angular orientation of the birefringent element and x and y are the spatial coordinates of the birefringent element. Such tuning mechanism requires circularly polarized light and imposes two restrictions on the manipulated light: the phase profiles imparted on left circularly polarized (LCP) light and on right circularly polarized (RCP) light are equal and opposite in sign [that is, $\phi_{LCP}(x, y) = -\phi_{RCP}(x, y)$], and the handedness of polarization reverses upon reflecting off or transmitting through the metasurface.

Dielectric metasurfaces are normally constructed by a periodic or another deterministic arrangement of high index subwavelength dielectric scatterers (or its inverse). However, they should not be confused with photonic crystals, which are also made as periodic arrays of scatterers. Dielectric metasurfaces' function relies on the collective optical response of individual constituent building blocks to form the desired wavefront in the far field. Therefore, dielectric metasurfaces are radiative in nature, whereas photonic crystals are built on constructive and destructive inference from periodic dielectric elements and solely rely on diffraction. Because of this difference, dielectric metasurfaces and photonic crystals can be distinguished by their Mie resonance wavelength (λ_{Mie}, controlled by dielectric constant of nanoparticles) and Bragg resonance wavelength (λ_{Br}, controlled by lattice periodicity): when $\lambda_{Mie} > \lambda_{Br}$, Mie scattering dominates in dielectric nanoparticles and the periodic collection of dielectric nanoparticles form a metasurface; when the period is increased such that $\lambda_{Mie} < \lambda_{Br}$, the structure enters photonic crystal regime [83]. From an experimental perspective, 2D metasurfaces are usually irradiated at angles normal to the plane of the metasurfaces (or at reasonably small angles with respect to the normal axis) and operate in reflection or transmission modes. In contrast, the in-plane guided modes in 2D photonic crystals are usually launched in the plane of the periodic arrays by optical couplers, and cannot be miniaturized [84].

4 Emerging material platforms for optical metasurfaces

In the previous sections, we have discussed the fundamentals of plasmonic and dielectric metasurfaces. We will review in detail the progress made with different materials (listed previously in Table 1) as building blocks for metasurfaces catering to specific applications.

4.1 Refractory plasmonic materials

As discussed previously, plasmonic and nanophotonic metasurfaces have grown continuously and found application in a wide variety of optical elements. The two most typically used materials for plasmonic metasurfaces are gold and silver. These materials suffer from many limitations when considered for practical devices. They are incompatible with operations that require temperature stability, robustness to high-intensity lasers, chemical inertness, ultrathin films, and CMOS compatibility. In this application space of plasmonics, the emerging transition metal nitrides become essential. Here, we discuss their relevance to metasurface-based devices. In 2011–2012, titanium nitride (TiN) and zirconium nitride (ZrN) were first reported for their usefulness in plasmonics [80, 116]. Visually, TiN and ZrN resemble the appearance of gold (Au), suggesting a substantial similarity in their optical properties. Furthermore, these materials show chemical stability at temperatures beyond 2000°C, which classifies them as ceramics [80]. The plasma frequencies of both TiN and ZrN are in the visible range but typically exhibit a high $\mathrm{Im}(\varepsilon)$, i.e. relatively large optical losses in the visible and near-infrared (IR) spectrum as compared to commonly used noble metals (see Figure 2A,B). TiN has found ample uses as a cheap alternative to Au for metallic coatings and is already incorporated in standard CMOS processing [123,

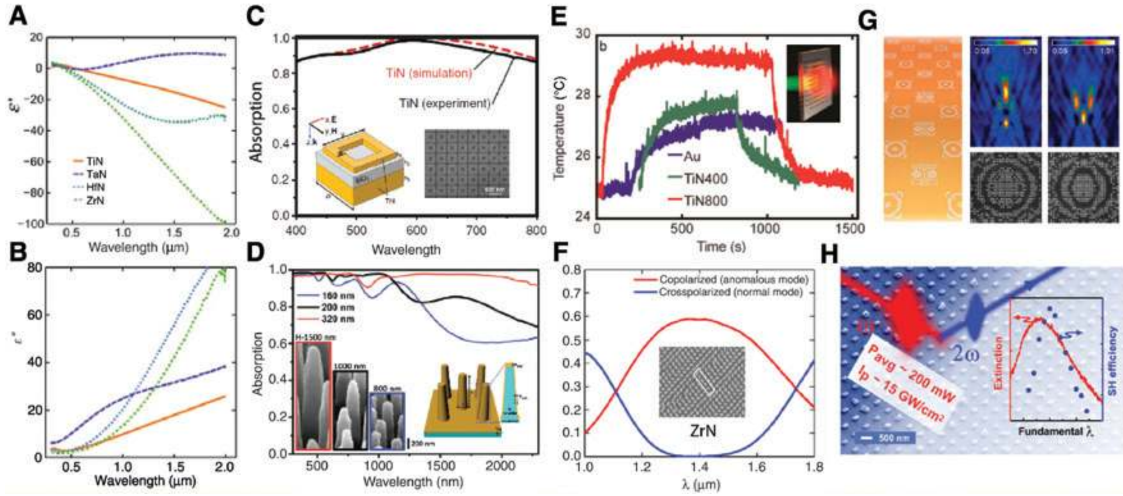

Figure 2: Examples of TiN based metasurfaces.
(A)–(B) Measured optical properties [real (A) and imaginary (B) parts of the dielectric permittivity] for various different transition metal nitrides, e.g. TiN, ZrN, hafnium nitride (HfN), and tantalum nitride (TaN) [80]. (C) Simulated (dashed line) and measured (solid line) absorption spectra for the TiN MM absorber. (Inset – left) Schematic representation of a unit cell of the three-layer TiN MM absorber with dimensions of $a=250$ nm, $w=50$ nm, $p=300$ nm, $h_1=30$ nm, $h_2=60$ nm, and $h_3=150$ nm; (inset – right) SEM image of the fabricated TiN absorber [117]. (D) Experimental absorption spectra of 3D truncated TiN nanopillar structures with 160, 200, and 320 nm diameters at their maximum achievable structure heights of 800, 1000, and 1500 nm, respectively. The inset represents the cross-section of the nanostructures [118]. (E) Time-dependent temperature of the sapphire substrate heated by plasmonic nano-disk array when excited by an 800-nm laser illumination. The inset shows schematic [119]. (F) Reflected power distribution between circular copolarized (red) and cross-polarized (blue) components as obtained in simulations for ZrN nanoantenna on bilayer stack of ZrN/AlScN to create a gap plasmon resonance. The inset shows a SEM image of a fabricated metasurface [120]. (G) (Left) TiN hole array lattice schematic, (middle – right) TiN lattices with a single hole size can simultaneously focus light on multiple regions, (lower) SEM images of TiN lattice optics, and (upper) the corresponding confocal microscopy images ($\lambda=800$ nm). The lattices were optimized to produce (left) two focal points at $x=\pm1$ μm, $y=0$, and $z=4$, 6 μm and (middle) two focal points at x, $y=0$, and $z=3$, 7 μm [121]. (H) Colored SEM image of the 180-nm-long rectangular TiN nanoantenna; schematic of the SHG and the inset shows measured second harmonic (blue) and the corresponding extinction spectra (red) [122]. (A) and (B) reprinted with permission from [80], copyright 2013 by John Wiley and Sons; (C) reprinted with permission from [117], copyright 2014 by John Wiley and Sons; (D) reprinted with permission from [118], copyright 2017 by John Wiley and Sons; (E) reprinted (adapted) with permission from [119], copyright 2013 by the American Chemical Society; (F) reprinted (adapted) with permission from [120], copyright 2016 by The Optical Society; (G) reprinted (adapted) with permission from [121], copyright 2013 by the American Chemical Society; (H) reprinted (adapted) with permission from [122], copyright 2016 by the American Chemical Society.

124]. Large-area nanofabrication techniques for plasmonic applications have also been established for TiN [125]. Although initially reported to be nonstoichiometric, TiN is capable of being grown for single-crystalline ultrathin plasmonic metal films [126]. Their temperature-dependent optical properties have also been studied, which has opened up doors for their application in high-temperature sensing devices [127].

In an early work, a TiN-based MM functioning as a broadband absorber was demonstrated [117]. Absorption higher than 87% is obtained for 400–600 nm spectral window for an array of square-ring-type TiN resonators on a bilayer stack of SiO_2 on TiN on a sapphire substrate (Figure 2C). This design utilized the lossy nature of the metal back layer at higher frequencies together with losses caused by LSPs in the square ring array toward the lower-frequency regime. In the same work, the authors also tested the structures for stability against high temperature and intense laser illumination. Recently, another demonstration of polarization insensitive, broadband absorption utilized plasmonic TiN coating on an array of 1.5-μm-tall Si pillar structures. Almost 94% absorption of the incident illumination is achieved in the wavelength range of 300–2300 nm (Figure 2D). Later, additive atomic layer deposition (ALD) grown hafnium oxide (HfO_2 ~30 nm) coating was used on the TiN pillars to protect it from ambient oxidation, and as a result, thermal stability for temperatures up to 1473 K was also demonstrated.

In another example, local heat generation was explored by utilizing the surface plasmon resonances in the near-IR [119]. An array of disk-shaped TiN nanoparticles was shown to be an efficient nanoscale heat source that outperformed a similar Au-based counterpart in the biological transparency window (Figure 2E).

Nanoparticles are vital components of many essential device applications of plasmonics. Single-crystalline colloidal plasmonic TiN nanoparticles have been examined early on, identifying them to be particularly useful in photothermal, photocatalytic, and nanoscale heating systems [128, 129]. Recently, researchers have also demonstrated efficient broadband hot electron generation and collection mechanism in TiN-nanoparticle-decorated TiO_2 nanowires [130]. Broad plasmonic resonances in TiN nanoparticles produced higher photocurrent enhancement in solar water splitting as compared to the Au nanoparticle counterparts.

The first demonstration of high-efficiency phase-gradient metasurface using refractory metal nitride used ZrN brick antenna structures on a bilayer plane of AlScN (aluminum scandium nitride) on ZrN [120]. This metasurface exhibits PSHE by creating a spatially separated mirror symmetric spectrum of the two opposite circular polarizations (right and left) of the incident light (Figure 2F). High working efficiency (~60%) similar to a previously reported Au-based design was achieved.

In yet another recent work, a metasurface device has been designed using subwavelength hole arrays in single-crystalline plasmonic TiN [121]. A powerful lattice evolution algorithm was implemented that utilized inverse form fitness function-based multiobjective optimization method. The resulting design of large area nanohole lattice in TiN could produce arbitrary far-field light patterns with balanced intensities at the wavelength of ~800 nm (Figure 2G).

Elevated damage threshold makes the refractory metal nitrides suitable for nanophotonic applications of nonlinear effects. Direct Z-scan measurements on TiN films have concluded the effective nonlinearities similar in magnitude to other standard metal films [131]. Low second harmonic intensity has also been previously measured from TiN thin films [132]. However, a significantly high laser power (5 GW/cm^2) damage threshold has been experimentally verified for the thin films made of this metal nitride. More recently, in another work, second harmonic generation (SHG) was recorded from a rectangular array of TiN brick antenna structures with plasmonic resonances in the wavelength range of 950–1050 nm [122]. Compared to a similar Au-based design, TiN structures showed excellent stability and could endure laser intensities up to 15 GW/cm^2 without changing their optical properties or physical appearance (Figure 2H). Additionally, thin dielectric coated nanostructured Au has also been demonstrated useful for refractory plasmonics and nonlinear optics applications [77].

The studies discussed above have established the importance of TiN-based nanophotonic devices in numerous applications to harsh environment operating systems such as solar thermophotovoltaics, combustion thermophotovoltaics, waste heat harvesting in industries, as well as for durable optical elements for high power laser application, e.g. nonlinear signal converters, biological and chemical sensors, photocatalysis, HAMR, and so forth.

4.2 Epitaxial silver

As mentioned previously in the plasmonic metasurfaces section, silver has the highest negative permittivity in the visible frequency regime, which makes it suitable for plasmonic application. However, a silver thin film that is grown with electron beam evaporation often has poor optical properties as the film is not lattice matched to the substrate and is usually polycrystalline. For thin films that are subwavelength thick, the optical properties in the visible frequencies become less plasmonic and lossier due to the grain boundary defect scattering. An epitaxially grown silver thin film has the potential of having plasmonic properties similar to bulk silver films at a reduced thickness. Lattice matching of silver with substrates such as alumina (Al_2O_3), magnesium oxide (MgO), or mica is well known in the literature [133, 134]. The epitaxial silver film was explored for plasmonic application by Park et al. [135] on Mica substrate and patterned using focused ion beam (FIB). Wu et al. [136] demonstrated an epitaxially grown silver thin film on heavily doped Si substrate. Epitaxially grown silver thin film is shown to have an order of magnitude smaller root mean squared (RMS) surface roughness than that of equivalent thermally evaporated silver thin film. The 45-nm silver thin film had comparable optical properties of bulk silver films of Johnson and Christy [137]. Using a capping layer of Al_2O_3, they experimentally showed a surface plasmon polariton (SPP) propagation distance of 42 μm at 880 nm wavelength while theoretically calculating a 155 μm propagation distance for an ideal layer of film.

From measured optical constants of their thin film, Wu et al. numerically computed and showed that epitaxial silver nanostructures have the potential to exhibit a much sharper Fano-resonance than similar structures made from the evaporated silver film. Figure 3A shows experimentally obtained propagation length for epitaxial silver films, as well as numerical simulation results showing epitaxial silver outperforming evaporated silver with sharper Fano resonance and enhanced surface-enhanced Raman scattering (SERS). Numerical calculations show that for

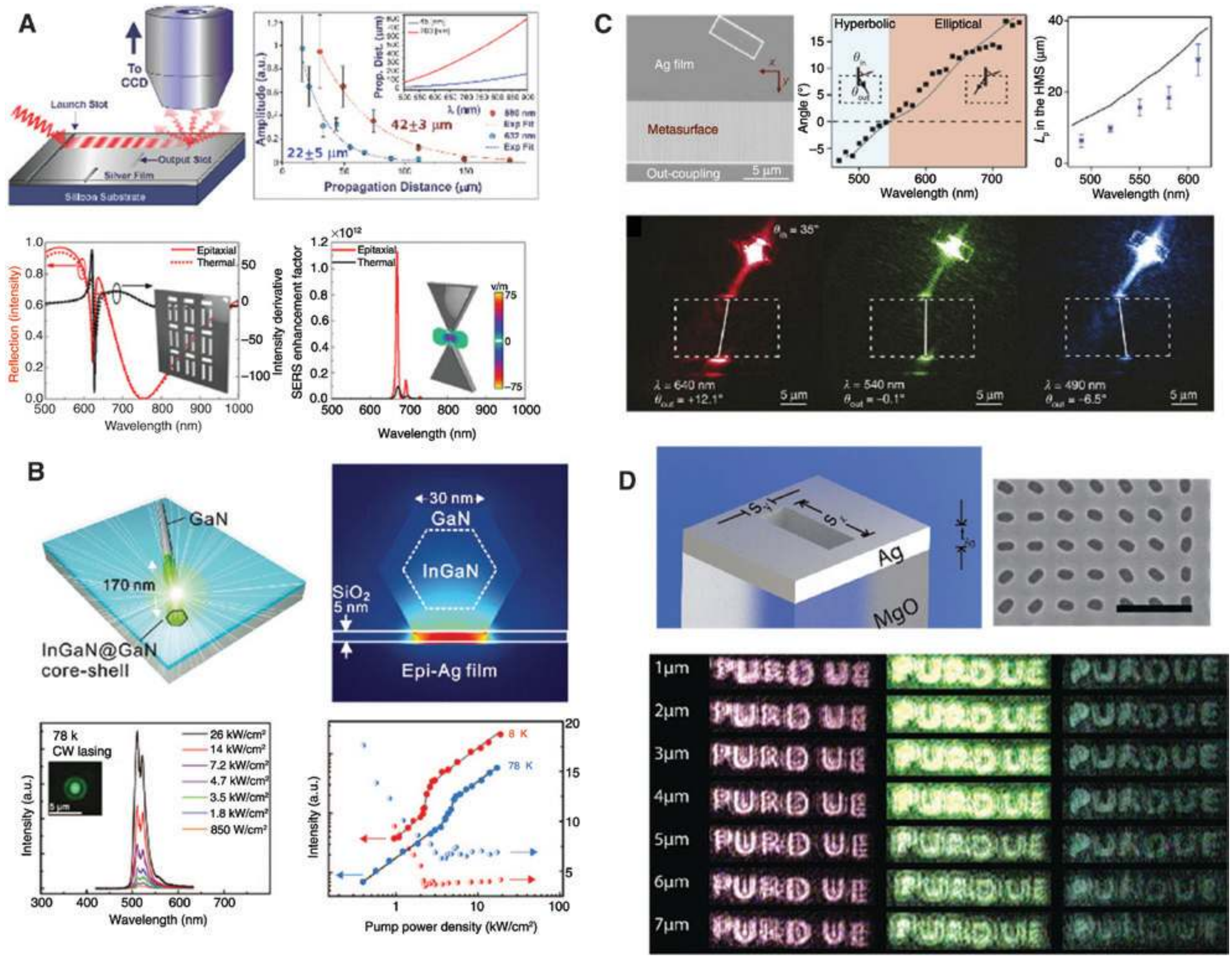

Figure 3: Epitaxial silver for metasurface applications.
(A) Epitaxial silver shows sharper Fano resonance or enhanced field confinement in bow-tie antenna compared to their evaporated counterparts [136]. Top-left panel shows experimental setup with SPP waves launched in the silver thin film. Top-right panel shows the propagation distance for different amplitudes obtained experimentally. Bottom-left and bottom-right panels show the theoretical calculation for Fano-resonant and SERS enhancement factor for epitaxial and thermally evaporated silver. (B) Epitaxial silver mirror reduces mode volume of lasing [138]. The top-left panel shows the GaN-InGaN core-shell structure, and top-right shows the field enhancement in SiO_2 spacer layer with the epitaxial silver thin film. Bottom-left shows the emission spectra with different pump fluences and bottom-right shows the lasing saturation. (C) Hyperbolic dispersion in 2D structure demonstrated with the help of epitaxial silver [139]. Top-left panel shows the SEM image of the device, and the top-middle panel shows the deflection angle as a function of wavelength. Below 550 nm wavelength, the device shows negative refraction and therefore operates in the hyperbolic regime. Top-right panel shows the propagation length in the hyperbolic metasurface. The bottom panel shows optical images of the refraction in three different wavelengths of 640 nm, 540 nm, and 490 nm. (D) Color holography with epitaxial silver metasurface [40]. Top-left shows a schematic of a single unit cell, while top-right shows a SEM image, with scale bar representing 500 nm. The bottom panel shows optical images with objective focused at different distances from the metasurface. At 5 μm distance, the image appears to be clearest. (A) Reprinted with permission from [136], copyright 2014 by John Wiley and Sons; (B) reprinted with permission from [138], copyright 2012 by the American Society for Advancement of Science; (C) reprinted with permission from [139], copyright 2015 by Springer Nature; (D) reprinted with permission from [40], copyright 2017 by John Wiley and Sons.

core-shell structures [136] with the gain medium, epitaxial silver can obtain normalized polarizability necessary for the lasing condition, where thermally evaporated silver cannot. For bow-tie antennas made of silver, they numerically predicted that epitaxial silver bow-ties would have 16 times SERS enhancement factor at resonance than evaporated silver-film-based structures.

A direct comparison between evaporated and epitaxial silver was performed for lasing application by Lu et al. [138] that showed the superior performance of epitaxial silver. An epitaxial silver film is used as a back-reflector layer, and a 5-nm-thin spacer layer of SiO_2 is situated between InGaN@GaN core-shell structure and the silver back-mirror. FEM simulation shows strong field confinement in the spacer layer. With 405 nm CW semiconductor diode laser excitation, lasing at 510 and 522 nm was observed. In contrast, a similar InGaN@GaN core-shell structure with a similar thickness of SiO_2 but on a polycrystalline (evaporated) silver showed no lasing. Figure 3B shows high mode confinement using the epitaxial silver structure. It is evident that the epitaxial silver is critical to demonstrate lasing using the structure. Bimodal lasing with similar pumping threshold was experimentally observed.

It was predicted that hyperbolic metasurface could show anomalous dispersion [140] for propagating SPP similar to a bulk 3D metasurface. In their letter, Liu et al. showed that a metasurface, when engineered adequately with periodic gratings, can give rise to flat or hyperbolic isofrequency dispersion contours. The so-called "hyperbolic metasurface" was first demonstrated through epitaxial silver by High et al. [139]. Their fabricated metasurface showed in 2D some of the critical characteristics of bulk hyperbolic MMs, such as negative refraction and diffraction-free propagation. Figure 3C depicts the negative angle of refraction at wavelengths lower than 550 nm, denoting the hyperbolic regime, and the positive angle of refraction at the elliptical regime with wavelengths longer than 550 nm. These devices demonstrated polarization-dependent spin-orbit coupling of incoming photons, which could readily showcase the PSHE.

Epitaxial silver's low loss and long SPP propagation length at the visible frequencies can be utilized to make metasurfaces for visible frequency applications. Since epitaxial silver is grain-boundary defect free, one can easily pattern the film using FIB, whereas for evaporated silver with grain boundaries, patterning causes rough side walls. Patterned rotated nanoslits can provide Pancharatnam-Berry geometric phase to an incoming electromagnetic wave. Again, for a hologram generation, one must use computed phase profile to reproduce an image to a virtual plane. By using the computed phase profile, rotated nanoslits are patterned onto an epitaxial silver film that gives incoming circularly polarized light the necessary phase shifts for creating the hologram. The resulting holograms are observed using confocal microscopy at a focal plane of 10 μm above the structures, as demonstrated in Figure 3 [40]. Figure 3D shows the observed holograms while the focal plane is shifted, showing the sharper image at the designed length of 5 μm.

Though silver itself is a conventional plasmonic material, epitaxial silver, having optical properties of bulk silver at nanoscale thicknesses, opens new dimensions for plasmonic metasurface design at visible wavelengths with strong field confinement and lower loss.

4.3 Silicon and its oxides and nitrides

Compared to plasmonic metasurfaces, dielectric metasurfaces has a clear advantage for low loss application. Section 3 discusses the principles of dielectric metasurfaces; in this subsection, many of the important works on silicon-based metasurfaces are listed. The primary advantage for silicon-based metasurface is the ability to use existing fabrication techniques and tools to manufacture the devices rapidly. Silicon has been the primary material of choice for the CMOS industry for over five decades. Since silicon manufacturing technology is robust, many of the proof-of-concept designs for dielectric metasurface chose silicon platform to demonstrate the concepts. Silicon is lossier than transparent dielectric materials in the visible-IR regime, and most devices that utilize silicon show operation in the near-IR regime. For an excellent overview of this topic and a possible future roadmap, please refer to Staude and Schilling's review [83].

High-efficiency dielectric Huygens' surfaces were proposed by Decker et al. [105], by spectrally overlapping the electric and magnetic resonances for Si nanodisks. By engineering the height and diameter of Si nanodisks, they overlapped the two resonances of the nanodisks. Figure 4A inset shows the array of Si nanodisks. The simulation results in Figure 4A illustrate that by adjusting the disk radius, the phase control of 2π can be achieved. For near-IR operation, the experimental results are shown in Figure 4B, which shows near-unity transmission with phase dependent on the incoming frequency.

Dielectric resonators with silicon were demonstrated as a material platform by Yang et al. [53]. They designed the metasurface by maximizing the cross-polarized reflection and choosing the dimensions of the silicon nanoresonator to obtain proper phase shift. By patterning silicon nanoantennas backed by a silver reflector, vortex beam generation at a conversion efficiency of 98% at 200 nm bandwidth is shown. Figure 4C shows an optical image of the vortex plate. Yang et al. [87] also showed a cloaking effect using the all-dielectric silicon-based metasurface. Figure 4D shows near-unity transmission in telecommunication wavelength for the designed all-dielectric metasurface. They showed that the EIT device could easily outperform its plasmonic counterpart and could be used for refractive-index sensing with a higher sensitivity and figure-of-merit than its plasmonic counterparts. Figure 4E shows refractive index sensing using a Fano resonance Si metasurface. Moitra et al. [89] demonstrated high-efficiency perfect reflector using Si material platform by utilizing the Mie resonance. The array of Si nanodisks shows

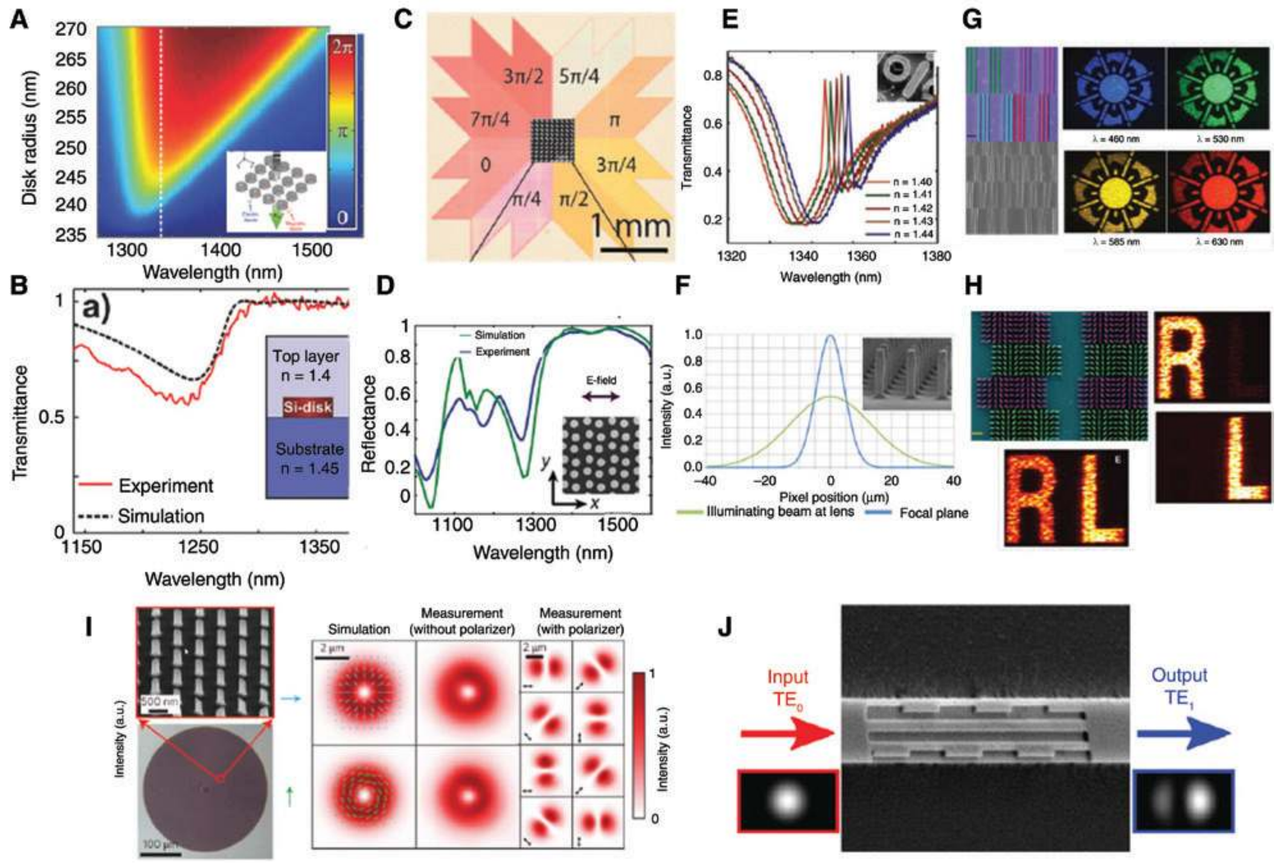

Figure 4: Silicon as a metasurface material platform.
(A) Computed phase profile of Si nanodisk array at different wavelengths and diameters of disks show full 2π phase control (inset: Si nanodisks engineered to have simultaneous electric and magnetic resonance). (B) Near-unity transmittance for the disk array shown both with simulation and experimental results [105]. (C) Optical image (inset: SEM image) of a Si vortex plate [53]. (D) Si-metasurface-based perfect reflector [89]. (E) Refractive index sensing using Si-based Fano-resonance metasurface [87]. (F) Enhanced focusing with the Si-based flat lens (inset: SEM image of the Si-based flat lens) [141]. (G) Si-metasurface-based broadband holography; subpanels show SEM image and hologram in different illumination wavelengths. (H) Top-left: false-colored SEM image of chiral metasurface made of Si; purple and green colors represent two different chiralities. Right panels: R and L image represent right-hand circularly polarized (RCP) and left-hand circularly polarized (LCP) illumination response. The bottom-left panel shows unpolarized light response [112]. (I) Left panel shows optical and SEM images of Si nano-post-based metasurface; right panel shows beam conversion output, both simulation and experimental results [142]. (J) Metasurface grating embedded into a silicon waveguide show mode conversion. TE0 mode is converted into TE1 mode [143]. (A)–(B) reprinted with permission from [105], copyright 2015 by John Wiley and Sons; (C) reprinted with permission from [53], copyright 2017 by the American Chemical Society; (D) reprinted with permission from [89], copyright 2014 by the American Physical Society; (E) reprinted with permission from [87], copyright 2014 by Springer Nature; (F) reprinted with permission from [141], copyright 2014 by the Optical Society of America; (G)–(H) reprinted from [112] through Creative Commons Attribution-NonCommercial license from Science Advance; (I) reprinted with permission from [142], copyright 2015 by Springer Nature; (J) reprinted with permission from [143], copyright 2016 by the American Chemical Society.

98% reflectivity in 200 nm bandwidth at the near-IR wavelength.

Silicon nanoposts have been utilized to create an on-chip focusing lens by West et al. [141] where the nanopillars were fabricated using reactive-Ion etching on a silicon wafer. Figure 4F shows a SEM image of the structures of the lens and focusing of a Gaussian beam. Full phase control was achieved at telecommunication wavelength of 1.55 μm. Designed silicon lens showed subwavelength thin micro-lens effect. Such lenses could be used for reducing insertion loss by wafer-level integration of the lens. Kim et al. [144] demonstrated phase control and focusing by patterning nano-apertures in a silicon substrate. They showed the achromatic performance of the designed lens at operating wavelength of 1500–1900 nm. Khorasaninejad et al. showed aberration-free imaging by metasurface lens by patterning coupled dielectric resonator array. Invariance of focal length is demonstrated experimentally from 1300 nm to 1800 nm wavelength for their lens. By utilizing their Si platform, Khorasaninejad et al. demonstrated dispersion-free broad-band and chiral holograms with blazed-binary silicon grating structures and rotated nanoantennas [112]. Figure 4G demonstrates the broad-band hologram operating at 480, 530, 585, and 630 nm. Figure 4H shows the false-colored SEM image of the chiral hologram. Magenta and green represent the two chiralities. Figure 4H shows the output of the metasurface, while R is displayed when RCP light is illuminated on the device, and L is displayed for LCP light.

Arbabi et al. [142] showed high-efficiency metasurface with silicon by utilizing high contrast Si nanoposts. Each nanopost acts as a low-Q Farby-Perot resonator, while the orientation of ellipse determines the polarization-dependent phase shift of the structure. Experientially, up to 97% efficiency was shown for such metasurfaces. Figure 4I shows the optical microscopy and SEM image of such metasurface and illustrates both experimental and simulation results for an axial and radial polarization converter with the metasurface.

Recently, a high-efficiency Si-metasurface with crystalline Si was reported by Zhou et al. [145]. By transferring thin-film c-silicon onto a quartz substrate and patterning it with electron-beam lithography into nanoposts, they created Si metasurface on transparent substrates. They showed that the crystalline Si metasurface could obtain transmission efficiency of 71% and 95% diffraction efficiency with full 2π phase control at 532 nm wavelength.

The primary advantage of Si metasurfaces is that they can augment or modify the existing devices and bring in new applications. All dielectric chiral metasurface with CMOS compatible process was demonstrated with silicon with a quality factor of up to 100 [146]. Vortex converter with 45% efficiency at telecommunication wavelength is shown using Si [107]. Mode conversion was demonstrated with the help of metasurfaces embedded on a silicon waveguide [143, 147]. Figure 4J shows the SEM image and input and the output for such a device. The fabricated SOI structure can readily convert a TE0 mode to the TE1 mode using graded refractive index profile. The measured mode purity is shown to be 95% for the transformed mode and transmission of 88% is achieved. Enhanced nonperturbative high-harmonic emission from is demonstrated with a Si metasurface designed with Fano-resonance [148].

Silicon compounds such as silica (SiO_2) and silicon nitride (Si_3N_4) are both transparent in the visible and has lower losses and can be suitable for metasurface fabrication. Si_3N_4 has a higher refractive index of 2.032 compared to around 1.5 for SiO_2 and therefore can give better index contrast. Both SiO_2 and Si_3N_4 have lower indices than TiO_2, which has been explored more for metasurface fabrication and is further discussed in Section 4.4. Si_3N_4 has been utilized to make low-contrast metasurface with high transmission efficiency and focusing efficiency [149]. Park et al. [150] showed subtractive color filter with cyan, magenta, and yellow color with hydrogenated amorphous silicon (a-Si:H) disks, which shows potential to generate full-color pallet with such devices. Unpolarized high-numerical-aperture imaging with Si_3N_4 lens has also been experimentally demonstrated [151]. Planar a-Si metasurface embedded into SiO_2 was made by local oxidation of silicon [152] and reflects the viability of combining the silicon platform with its nitride and oxides.

4.4 Titanium dioxide

One major potential application of metasurface is to construct flat metalenses to realize focusing and imaging functionalities. Such lenses can be made with wavelength-comparable thicknesses, as opposed to their refractive counterparts, which require large thicknesses to realize phase accumulation through light propagation in the material. To shape the wavefront into the desired form, metalenses are implemented by discretizing the flat surface into sub-wavelength pixels (optical antennas), each imparting the locally required phase shift by either resonant or wave-guiding effect [82, 153]. As discussed above in the Plasmonic Metasurface and Si Metasurface sections, although metals and silicon are widely used in proof-of-concept demonstrations for metasurface researches, they are not suitable for making optical metalenses due to the substantial optical losses in the visible frequencies. Instead, great research endeavor toward high-efficiency metalenses has been focused on titanium dioxide (titania, TiO_2) due to its minimal optical loss and high refractive index (~2.4) across the visible spectrum. The high refractive index results in large optical confinement inside the optical elements, which diminishes the optical crosstalk between neighboring elements when the spatial sampling period (i.e. pixel size) is reduced for higher efficiency. In fact, TiO_2 metalenses have been realized in as early as the 1990s. In a first effort known to date, Lalanne et al. [102–104] experimentally demonstrated 78–89% first-order diffraction efficiency at 633–860 nm wavelengths in a TiO_2-based binary blazed grating structure (Figure 5A). The beam diffraction was realized by patterning TiO_2 with variable fill fraction, thus local refractive index in each pixel, so that a distribution of effective refractive index could be engineered to achieve the desired beam diffraction. The pixel sizes were carefully chosen to optimize the performance while also accounting for fabrication limitations. The resulted diffraction efficiency was ~12% higher than that of conventional

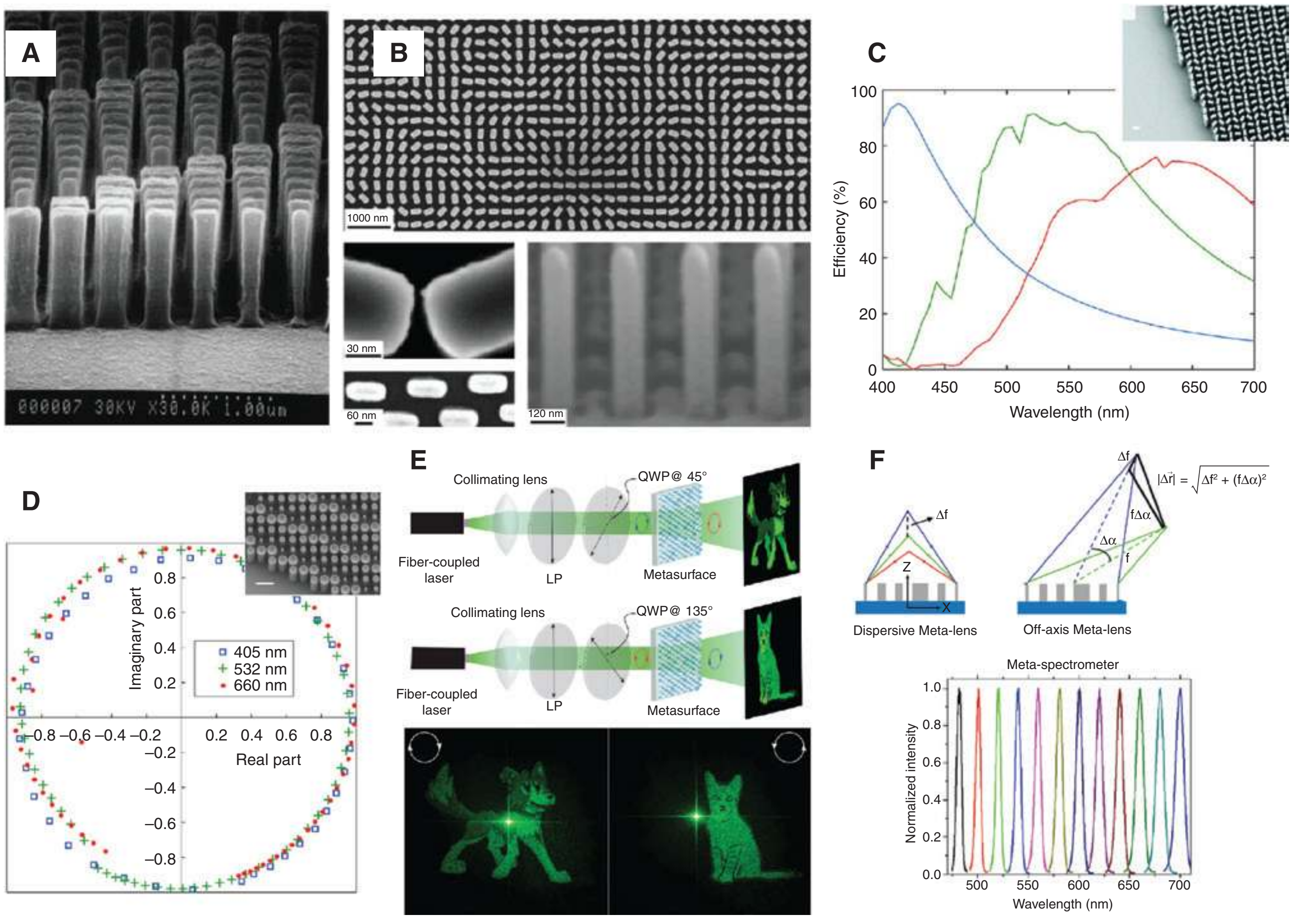

Figure 5: Titanium dioxide (TiO_2) as a metasurface material platform.
(A) Scanning electron micrograph (SEM) of a blazed binary diffractive lens made of top-down etched TiO_2 nanopillars; the local effective refractive index is controlled by the width of the pillars. (B) SEM of TiO_2 metalens fabricated using the bottom-up atomic layer deposition (ALD) method. Inset: Cross-section view of the nanofins exhibiting vertical sidewalls with a height of ~600 nm. (C) Simulated focusing efficiency of three metalenses designed for wavelengths 405 (blue curve), 532 (green curve), and 660 (red curve) nm and SEM of fabricated metalens. Inset: measured focal spot intensity at designed wavelength 405 nm (NA = 0.8). (D) Simulated complex transmission coefficients of cylindrical nanopillars with various diameters at three design wavelengths: 405, 532, 660 nm. Each point represents the amplitude and phase of the transmission of a nanopillar, and the entire 2π phase coverage is realized by varying the nanopillar diameter. (E) Top: different holograms are imaged with LCP and RCP light illuminating on the same TiO_2 metasurface, which decouples the propagation phase design and geometric (Pancharatnam-Berry) phase design by controlling the nanofin dimensions and rotation angles, respectively. Bottom: images formed with RCP and LCP light, respectively. (F) Left: schematic of the off-axis meta-lens that focuses light of different wavelengths to different angles. Right: measured spectra from a supercontinuum laser with a planar ultracompact visible chiral spectrometer designed based on the off-axis focusing lens; the performance is comparable to a commercial handheld spectrometer. (A) reprinted with permission from [103], copyright 1999 by The Optical Society; (B) reprinted with permission from [154], the authors; (C) reprinted with permission from [27], copyright by the American Association for the Advancement of Science; (D) reprinted with permission from [110], copyright 2016 by the American Chemical Society; (E) reprinted with permission from [155], copyright 2017 by American Physical Society; (F) reprinted with permission from [156], using the Creative Commons Attribution (CC BY) license.

echelette lenses (also known as the Fresnel lenses) because the adverse shadowing effect (abnormal light refraction close to the vertical edge of the blazed gratings) inherent to echelette lenses was amended with waveguiding effect in the TiO_2 metalens [104].

This field was recently revisited by a group of researchers at Harvard University, who used a novel ALD-based technique to fabricate TiO_2 nanopillars (referred to as "nanofins" in their publications) with aspect ratio as high as 15, nearly 90° vertical sidewalls, and roughness RMS as small as 0.738 nm [154]. As is shown in Figure 5B, the fabrication quality from this bottom-up etching-free approach surpasses that from the previously used top-down etching approach, and this new fabrication technique initiated a growing field of TiO_2-based metalens researches. In a pioneering work, Khorasaninejad et al. [27] designed, fabricated, and characterized a flat focusing lens with a high free space numerical aperture (NA) of 0.8, as well as diffraction-limited focusing with efficiencies of 86, 73, and 66% at 405, 532, and 660 nm wavelengths, respectively, outperforming the state-of-the-art commercial refractive lenses in both the focal spot size and profile symmetry; the imaging ability of the proposed flat metalens was also tested to be comparable to the bulk refractive lens (Figure 5C). In a later work, the NA was further increased from 0.8 to 1.1 by immersion method while maintaining a focusing efficiency of 50% [157]. These two metalenses rely on the rotation angles of the nanofins to locally impart the required phase shifts and work only for circularly polarized light. To overcome this constraint, Khorasaninejad et al. [110] demonstrated a polarization-insensitive metalens in the visible with similar NA and focusing abilities, by replacing birefringent nanofins with axisymmetric nanocylinders with varying diameters to attain the appropriate phase profile (Figure 5D). Apart from focusing metalenses, it has been pointed out that arbitrary phase profiles can be imposed on any two orthogonal polarization states by a single metasurface combining propagation phase design and geometric phase design (realized through varying the x-y dimensions and rotation angles of TiO_2 nanofins, respectively). Using the principle of geometric phase, a multiplexed hologram metasurface was shown that displays different images when the helicity of the illuminating circularly polarized light changes [155] (Figure 5E). Furthermore, a single metalens was designed for highly resolved chiral spectroscopy where the circularly polarized light of different helicities are focused to different spots upon passing through the metalens, eliminating the need for stacked and bulky optical systems to do the same job [158]. TiO_2-based metasurfaces were also used to demonstrate ultracompact spectrometers. Zhu et al. [156] designed a metasurface that strongly disperses focused light of different wavelengths to different angles, so that high spectral resolution can be realized in a single flat metasurface, in contrast to bulky conventional spectrometers, which depend on long propagation distances to separate the insufficiently dispersed light (Figure 5F). Specially designed TiO_2 metasurface can convert circularly polarized light into vortex beams, and researchers showed that the high versatility of the metasurface design enables the generation of vortex beams with arbitrary and even fractional topological charges (number of helical surfaces that constitutes the final helical mode), while exhibiting an absolute efficiency of 60%, which significantly surpasses that of metallic metasurfaces (8.4%) with similar functionalities [159].

It is worth noting that besides dry-etching and ALD-based fabrication methods, an e-beam evaporation and lift-off-based technique has also been investigated to fabricate TiO_2 metasurfaces. Using this method, a tunable TiO_2 metasurface on a stretchable substrate was fabricated and shown to exhibit 5.08% (0.96%) resonance red (blue) shift in the visible frequencies when 6% strain is applied transverse (parallel) to the polarization of incident light [160]; TiO_2 color filters have also been realized with full coverage of the red, green, blue colors in the reflection mode, and the relatively small pixel sizes are promising for bright, high-contrast, and high-resolution structural color generation [161].

The recent years have seen tremendous progress in TiO_2-based metasurfaces in terms of focusing with high efficiencies and large NA, multiplexed holograms, beam splitters for elliptically polarized light, ultracompact spectrometers, etc. To make more applicable devices based on this platform, future efforts should be spent on the following aspects:

Expanding the effective bandwidth: Currently, three different metalenses are needed to cover the entire visible spectrum; in real applications, however, a single lens should focus all visible light with high enough efficiencies.

Broadening the field of view: Images obtained with TiO_2 metalenses still suffer from a geometrical aberration, even at a single wavelength, probably due to the large NA.

Developing the mass-production technology: The current fabrication technique requires e-beam lithography and ALD deposition of TiO_2, which impose significant hurdle on the manufacturing cost and throughput. New technologies such as the nanoimprint need to be explored for mass production without compromising device quality.

4.5 Transparent conducting oxides and other metal oxides

Metal oxides (MOs) are a diverse set of heavily doped, wide-bandgap semiconductors that have shown great promise as alternative materials for metal-based metasurface and plasmonic applications [80, 162–164]. In contrast to many doped semiconductors, MOs support large charge donor densities – metal dopants and/or point defects – and have corresponding carrier concentrations as large as 10^{21} cm^{-3}. Their large bandgaps restrict interband absorption primarily within the ultraviolet and visible spectrum, making intraband absorption the dominant loss mechanism at IR wavelengths. When combined, these two properties make MOs behave as a low-loss Drude metal at IR frequencies and a potential alternative material candidate for plasmonic and metasurface application and devices. Furthermore, MOs are exceptionally tunable materials. The past few years have seen an explosion of research into the nonlinear optical properties of MOs driven by optical, electrical, and thermal sources [51, 165–168]. Here, we review recent and concurrent research and applications of MO materials for realizing low-loss and tunable plasmonic metasurfaces.

In general, MOs are well described using the Drude model. Within this description, the optical response of a MO transitions from dielectric to metallic at the crossover wavelength. To achieve near-IR crossover wavelengths, large carrier concentrations with simultaneous low effective electron masses are necessary. Indium tin oxide (ITO) was among the first semiconductors to achieve carrier concentrations of 10^{21} cm^{-3} and a plasmonic response at near-IR frequencies [169]. Gregory et al. [170] demonstrated one of the first MO MMs using both directly patterned and complementary ITO split ring resonator antennas (Figure 6A). Subsequent studies into other

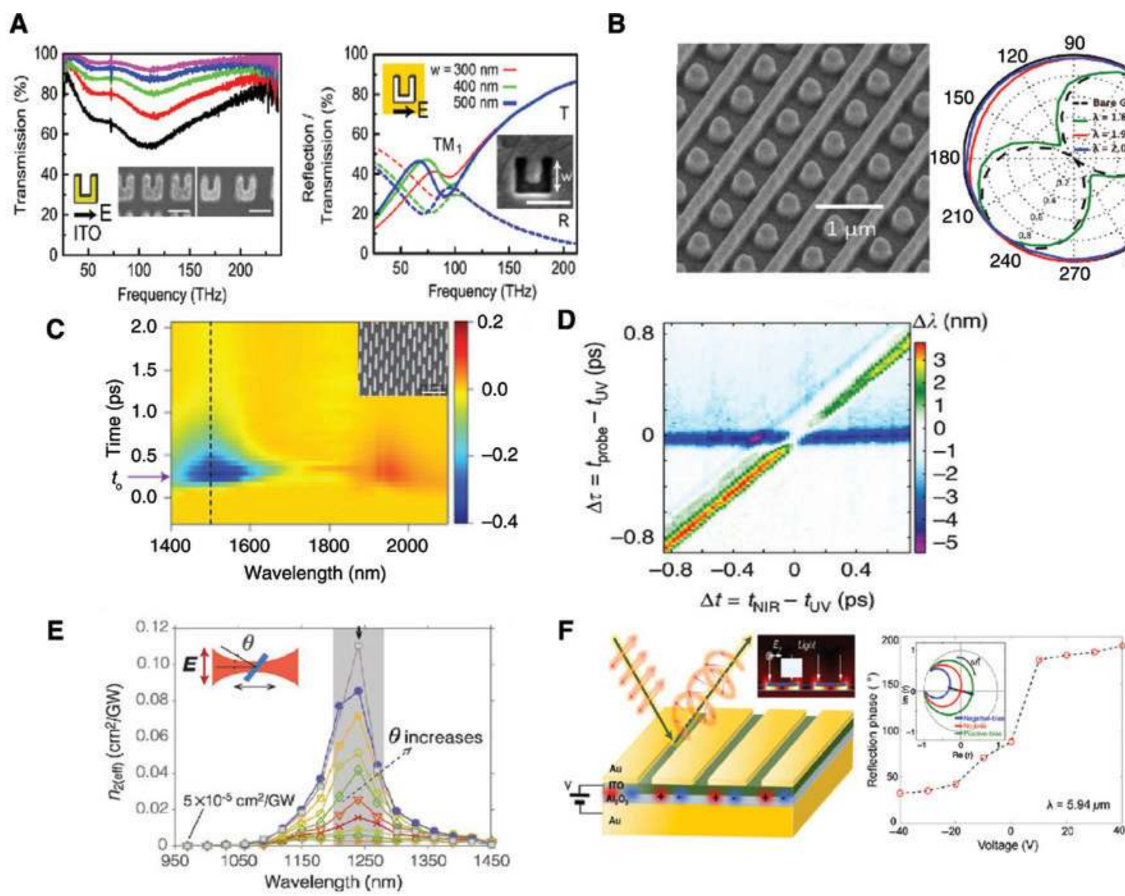

Figure 6: Transparent conducting oxides (TCO) as a metasurface material platform.
(A) IR transmission spectrum of direct (left) and complimentary (right) arrays of ITO nanoantennas showing plasmonic resonance dips. Insets show scanning electron micrographs of the fabricated ITO antennas. (B) Fabricated Ga:ZnO metasurface for near-IR (1.75–2.5 μm) quarter waveplate operation. Polar plot shows the intensity of reflected light after passing through a polarizer, demonstrating the linear to circular polarization conversion at the design wavelengths. (C) Ultrafast and broadband modulation of ITO nanorod arrays. The modulation amplitude exceeds 60% and recovers in less than a picosecond. (D) Ultrafast nonlinear wavelength shift of Al:ZnO thin films subject to both interband (UV) and intraband (NIR) pump. The two pump excitations induce opposite changes to the wavelength shift of the films and, when simultaneously combined, can completely cancel. (E) Enhance nonlinear effective refractive index of an ITO film at the ENZ wavelength of 1240 nm. Wavelength-dependent Kerr coefficient is measured using Z-scan and shows a clear enhancement at the ENZ wavelength, which increases drastically for increasing angles of incidence. (F) Electrically tunable metasurface arranged from plasmonic gap resonators. The voltage applied to the electrical contacts of the gold backing layer and gold antenna strips confines electrons at the ITO/Al_2O_3 interface. The accumulated electron density shifts the plasma frequency of the ITO layer and provides the necessary modulation functionality. Here, the authors were able to induce a dynamic 180° shift to the phase of reflected light. (A) Reprinted with permission from [170], copyright 2015 by the American Chemical Society; (B) reprinted with permission from [51], copyright 2016 by the American Chemical Society; (C) reprinted with permission from [171], copyright 2016 by Springer Nature; (D) reprinted with permission from [165], under terms of the Creative Commons CC BY license; (E) reprinted with permission from [166], copyright 2016 by the American Society for Advancement of Science; (F) reprinted with permission from [167], copyright 2017 by the American Chemical Society.

doped semiconductors quickly expanded the list of available oxides capable of supporting large carrier concentrations [80]. Kim et al. [172] demonstrated near-IR localized and surface plasmon resonances in periodically patterned aluminum- and gallium-doped zinc oxide (Al:ZnO and Ga:ZnO, respectively) films. In more advanced designs, the same authors fabricated Ga:ZnO/ZnO lamellar nanodisks for a highly sensitive mid-IR chemical sensor and also fabricated a Ga:ZnO quarter-waveplate operating at near-IR frequencies (Figure 6B) [51, 173].

Although MOs can themselves be designed as the metallic constituents of a metasurface, noble metals continue to outperform MOs for plasmonics because of their outstanding optical properties. However, MOs exhibit very large optical tunability, a quality that is not found in noble metals. The exceptional tunability of MOs was first highlighted and pioneered by the group of Otto Muskens. In 2011, Abb et al. [174] showed that the optical properties of gold antennas on an ITO substrate could be significantly modified on an ultrafast timescale by optically pumping at the resonance wavelength. This effect was attributed to the excitation and injection of free carriers into the ITO layer via the large electric fields of the antenna, which then modified the dielectric constant of ITO and shifted the antenna resonance. The authors extended their results by patterning multifrequency crossed antenna arrays onto an ITO substrate and demonstrated control over the fast Kerr nonlinearities and the slow thermal nonlinear contributions [175]. Metzger et al. [176] utilized the large nonlinearities of ITO nanocrystals placed in the gap of a gold dimer plasmonic antenna to enhance significantly the third-harmonic signal of the hybrid antenna structure. The group of Robert Chang showed large modulation amplitudes and picosecond recombination rates in 2D arrays of ITO nanorods [177, 178]; in 2016, this same group broke their previous record and reached subpicosecond recombination rates in their report of arrays of ITO nanorods operating at visible wavelengths (Figure 6C) [179]. Conformal coating of phase-change material was used to achieve broadband all-optical switching [180]. Clerici et al. [165] used films of aluminum-doped zinc oxide (Al:ZnO) to show that the ultrafast response in their MO films could be achieved with both intraband and interband pump energies and, furthermore, that the combined nonlinear response could be additively combined to achieve switching speeds up to a few terahertz (Figure 6D). Several groups have also demonstrated remarkable modulation enhancement of MOs near their epsilon-near-zero (ENZ) wavelength – the frequency at which the permittivity of the media is approximately zero [181–183]. In 2016, the group of Robert Boyd demonstrated enhancement factors of ~2000 for the Kerr nonlinear coefficients of ITO films by utilizing the field discontinuity property of ENZ materials (Figure 6E).

ITO thin films have also been demonstrated as efficient modulators [168, 184–186]. Huang et al. [186] showed a gate-tunable metasurface capable of generating a 180° phase shift and ~30% change in reflectance with a 2.5 V gate bias. Here, the authors fabricated 2D arrays of gold stripes on an aluminum oxide/ITO/gold layered substrate and applied voltage between sets of three antenna stripes and the gold back contact. The field effect at the aluminum oxide/ITO layer generated a substantial change in the refractive index of the ultrathin ITO layer and allowed for control of the metasurface reflectance amplitude and phase. Park et al. [167] also utilized a very similar design and reported an electrically controlled metasurface capable of 180° phase control. Here, the voltage was applied to the ITO layer and the gold back contact, eliminating the need to apply a voltage to individual or sets of antennas (Figure 6F).

4.6 Graphene and 2D materials

Since its successful cleavage from bulk graphite in 2004, graphene – a monolayer of carbon atoms arranged in a 2D hexagonal lattice [187, 188] – has been intensively investigated as a plasmonic material. While the high optical losses and lack of dynamic tunability hinder conventional noble metal plasmonics from practical applications, graphene is perceived to be the ideal candidate to overcome these hurdles owing to its unique electrical and optical properties. Before experimental demonstrations of graphene plasmons were carried out, theoretical calculations conducted by multiple groups suggested that graphene plasmons exhibit two enticing features: ultrahigh optical confinement on the order of several hundred ($\lambda_{air}/\lambda_{plasmon} \sim 100$) and long SPP propagation lengths (more than 100 SPP wavelengths in the mid-IR frequencies) [189–191]. These two features, together with graphene's dynamic tunability in optical properties, form the basis of the unique graphene plasmon platform with merits unparalleled by conventional noble metal plasmons. However, the substantial difference between free space wavelength and plasmon wavelength imposes a significant challenge to launch surface plasmons in graphene (Figure 7A). Launching plasmons requires sharp tips (with a radius of a few tens of nanometers) to excite SPPs [197–199] or nano-patterning graphene into metasurface to excite LSPs [192, 193, 195, 200–206]. Several early theoretical works on graphene metasurface applications

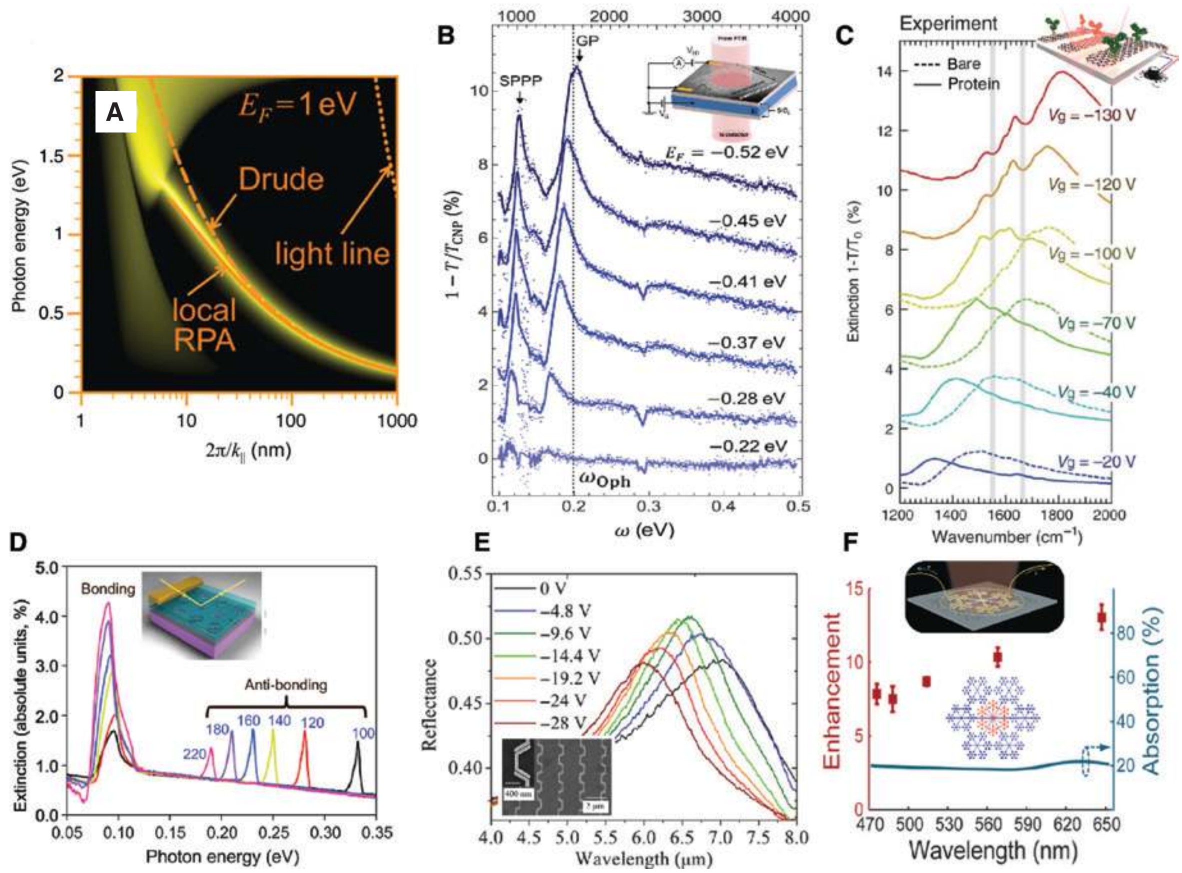

Figure 7: Graphene as a metasurface material platform.
(A) Calculated plasmon dispersion relation in graphene with Fermi level of $E_F = 1$ eV as a function of in-plane wavelength $2\pi/k_{\|}$. The light line (dotted curve) and the plasmon dispersion relations in the Drude (dashed curve) and local random phase approximation (local-RPA, solid curve) models are shown for comparison. The density plots are obtained using the full RPA conductivity for graphene with mobility $\mu = 2000$ cm^2/(V·s). (B) Measured extinction spectra of 50-nm-wide graphene nanoribbons at varying Fermi levels. The dotted vertical line indicates the energy of the in-plane optical phonon of graphene. Greater than 100× wavelength confinement ($\lambda_p \leq \lambda_0/100$) is achieved in 20-nm-wide nanoribbons with $E_F = 0.21$ eV (shown in a separate graph from the reference). Inset shows the schematic of FTIR spectroscopy measurement. (C) Measured extinction spectra of protein sensor consisting of graphene nanoribbons array before (dashed) and after (solid) protein bilayer formation. Gray vertical strips indicate amide I and II vibrational bands of the protein. This graphene protein sensor exhibits 6× sensitivity in a spectral shift and 3× sensitivity in spectral modulation (dips at the two vertical strips) compared to conventional gold plasmonic antenna sensors (shown in a separate graph from the reference). Inset shows schematic of graphene nanoribbon graphene sensor. (D) Measured extinction spectra for nanorings with various outer diameters with a fixed inner diameter (60 nm), as shown by labels. Note that the antibonding mode plasmonic resonance energy reaches up to ~0.34 eV in 100 nm outer diameter graphene nanoring. Inset shows schematic of the device. (E) Measured reflectance spectra from a graphene loaded gold plasmonic antenna array for different gating voltages ($V_G - V_{CNP}$; V_{CNP} is the gate voltage when the concentrations of electrons and holes in the graphene sheet are equal), showcasing the considerable dynamic tuning range (1100 nm) of plasmonic resonance caused by graphene. All spectra are normalized to the reflection spectrum from a 300 nm Au film evaporated on the same substrate. Inset: SEM of the gold plasmonic structure, the graphene sheet is underneath the gold antennas and is in the background of the SEM. (F) Measured photovoltage generation enhancement on fractal metasurface compared to plain source-drain contact. A rather broadband enhancement is achieved with fractal metasurface, and the enhancement is insensitive to incident light polarization due to the hexagonal symmetry of the fractal metasurface (shown in a separate graph from the reference). Top inset: artistic rendering of fractal metasurface enhanced graphene photodetector; bottom inset: geometry of fractal metasurface used to enhance photovoltage generation in graphene. (A) Reprinted with permission from [192], copyright 2014 by the American Chemical Society; (B) reprinted with permission from [193], copyright 2013 by the American Chemical Society; (C) reprinted with permission from [194], copyright 2015 by the American Association for the Advancement of Science; (D) reprinted with permission from [195], copyright 2013 by the American Chemical Society; (E) reprinted with permission from [196], copyright 2014 by the American Chemical Society; (F) reprinted with permission from [66], copyright 2017 by American Chemical Society.

have suggested that LSPs in graphene nanodisks can lead to complete optical absorption in mid-IR in a Salisbury screen configuration [207], and graphene ribbons can be made into electrically modifiable waveguides with longer propagation distances and higher edge field confinement than conventional bulk metallic waveguides [205], etc.

Notably, a recent theoretical work pointed out that ultrafast (~200 fs) radiative heat transfer happens in two graphene nanodisks vertically separated by 1 nm via plasmon interaction, resulting from the extraordinarily large plasmonic field concentration and low electronic heat capacity in graphene [208]. These theoretical works provided necessary tools to guide later experimental research on graphene metasurfaces.

Thanks to the development of nanofabrication technology, graphene metasurfaces with elements small enough to excite graphene plasmons were successfully fabricated, and the experimental works [193, 195, 202, 203] that followed explored in great detail the nature of graphene plasmons. The metasurface configurations used include graphene nanoribbons, nanodisks, and nanorings (Figure 7B–D). As the theory predicts, optical confinement more than 100, as well as plasmonic resonance tunability of 0.1 eV, has been experimentally achieved with LSP in graphene nanoribbons. It is worth noting that the confinement is much stronger than that obtained with SPP in unpatterned graphene sheet ($\lambda_{air}/\lambda_{plasmon} \sim 40–60$). The damping mechanisms of LSP in graphene nanoribbons via an interaction with graphene optical phonon and substrate phonon have also been investigated by several groups, revealing ~20 fs plasmon lifetime at energies above the optical phonon energy (~0.2 eV) of graphene [203]. Quite remarkably, resonance energies up to 335 meV (3.7 μm free-space wavelength) have been achieved in graphene nanorings [195]. However, it remains a significant challenge to further push the intrinsic graphene plasmonic resonance to near-IR and visible frequencies for telecom and detection applications. To accomplish this, nanostructures smaller than 5 nm and doping levels higher than 1 eV are required, and efforts are underway toward this goal. Theoretical calculations were also performed to support experimental results, where graphene was modeled either as a material with finite thickness (~0.3 nm) [193, 204] or as a surface current with zero thickness, which dramatically reduces computational cost [202]. Both numerical methods and analytical calculation [195, 204] achieved excellent agreement with experiments.

In addition to investigating the intrinsic graphene plasmons in graphene metasurface, researchers also used graphene to tune the plasmonic resonance in graphene/metal metasurface hybrid structures [209]. The idea is to make use of the tunable optical properties of graphene to dynamically change the environment dielectric function for the noble metal metasurfaces, therefore actively tuning their plasmonic resonances. It has been demonstrated that graphene can actively tune both the resonance linewidths [210] and frequencies [196, 211–214] in the mid-IR in back-gated graphene devices. The dynamic tuning range achieved reaches as large as 1.1 μm with a modulation frequency of 30 MHz [196] (Figure 7E), and 100% modulation depth was also shown in a tunable metasurface mid-IR perfect absorber [211]. For graphene to tune plasmonic resonances in near-IR and visible frequencies, gating voltages beyond typical dielectric breakdowns are needed to supply adequate carrier densities; therefore, alternative techniques to dielectric back gating are required. Emani et al. [215] demonstrated the electrical tunability of Fano-type resonance with graphene at ~2.4 μm with ionic gel top gating.

Based on the developments in the graphene-plasmon related works mentioned above, a number of applications utilizing dynamically tunable graphene plasmons with superior performance to conventional plasmonic material platforms have been realized. The following highlights some of the efforts.

Biosensing: Rodrigo et al. [194] showed that graphene nanoribbons exhibit 6× enhancement in sensitivity compared to gold dipole antennas when used to detect protein bilayers and that the resonance in graphene nanoribbons can be electrically tuned to sense difference vibrational bands (Figure 7C).

Photodetection: Noble metal metasurfaces [66, 216–220], as well as graphene nanoribbons [221, 222] have been used to enhance the sensitivity of graphene-based photodetectors by many research groups, and typically, the sensitivity can be improved by an order of magnitude (Figure 7F), even as high as by 200 times [217].

Lasing: Chakraborty et al. [223] showed that graphene could be used to dynamically tune the emission spectrum of quantum cascade lasers when placed on a metallic waveguide with aperiodic slits.

Optical absorber/modulator: Jang et al. [224] demonstrated tunable optical absorption (0–25%) with graphene nanoribbons in a Salisbury screen structure; Kim et al. [225] experimentally showed 28.6% transmission modulation efficiency by coupling graphene nanoribbons to metallic extraordinary optical transmission structure, whereas 95.7% modulation efficiency was predicted by calculations; graphene has also been demonstrated to be capable of light modulation in plasmonic slot waveguides, which are promising for ultracompact optoelectronic devices [226–228].

Since the successful exfoliation of monolayer graphene, the discovery of other 2D materials has surged. Among these 2D materials, phosphorene (black phosphorus) and transition metal dichalcogenides (MoS_2, WS_2, WSe_2, etc.) have been shown to exhibit outstanding quantum emission properties and plasmonic response [229–232], which make them promising candidates for metasurface applications. In addition, noble metal plasmonic structures were integrated with various 2D materials to enhance optical absorption and photon emission properties, as is in graphene/metal hybrid structures [233, 234]. To date, the relatively small sizes of exfoliated flakes of these 2D materials pose technological challenges to pattern them into metasurfaces; however, this field remains an active area of research because of the large wave confinement and dynamic tunability exhibited by the surface plasmons in such 2D materials [235–240].

4.7 Phase transition/change materials for tunable metasurfaces

Next-generation metasurface systems and devices will require efficient, dynamic, and programmable functionality to realize complete and versatile control of electromagnetic radiation. Phase transition and phase change materials (PTMs and PCMs) are a promising and emerging class of photonic materials that offer outstanding optical modulation performance across a wide breadth of control inputs, such as thermal, electrical, and optical excitations [241]. Their exceptional properties are well studied and have been utilized for a variety of applications well before their introduction into photonics [242]. Broadly speaking, the distinction between PTMs and PCMs is whether the process reverses naturally: PTMs are naturally reversible or, equivalently, volatile and will return to their initial, unperturbed state after a period of time if left unaltered; in contrast, PCMs are irreversible, that is, nonvolatile, and will remain in a fixed state of matter unless an input excitation "resets" the PCM back to its original state. Both volatile and nonvolatile processes have advantages and disadvantages for photonic applications. In this section, we discuss and review two prominent materials that have shown great promise for tunable metasurfaces, namely the volatile PTM vanadium dioxide (VO_2) and the nonvolatile PCM germanium-antimony-tellurium (GST).

At room temperatures, vanadium dioxide is in its insulating phase with a ~0.7 eV bandgap and a monoclinic crystal structure. If the temperature of VO_2 increases past the insulator-metal-transition (IMT) temperature – typically 340 to 345 K – the crystal structure becomes tetragonal rutile and the resistance decreases by nearly four orders of magnitude. The colossal change in resistance is associated with a corresponding modification of VO_2's dielectric permittivity $\varepsilon(\omega)$. Upon cooling, VO_2 will return to its insulating phase, but at a temperature lower than the IMT temperature, i.e. the cyclic transition exhibits hysteresis. In addition to thermal sources, switching between insulator and metal phases can be triggered with electrical, magnetic, or optical external perturbations. For optical-induced IMTs, the transition time can occur on the femtosecond time scale. These properties are what make vanadium dioxide such an attractive material platform for realizing tunable functionality in metasurfaces.

Initial studies of VO_2-based metasurfaces utilized arrays of split-ring resonators (SRRs) operating at IR frequencies. Driscoll et al. [243] patterned gold SRRs on a 90-nm film of VO_2 and monitored the resonance wavelength as a function of applied temperature. For temperatures higher than the IMT of 340 K, the sharp reduction in electric resistance of the VO_2 shorted the SRR's gap and shifted the 1.6 THz resonance frequency by up to 20%. In the following year, this same group demonstrated the very first "memory MM" [244] and circumnavigated the challenge using VO_2 for nonvolatile applications (Figure 8A). In addition to using a similar SRR + VO_2 metasurface design, Driscoll et al. attached electrodes to the VO_2 film to apply sequential 1-s electrical pulses and operated their device at maximum hysteresis to obtain persistent tuning via memory-capacitance. The resonance shift of the metasurface device could then be tuned in discrete, controllable steps.

Following the demonstration of SRR + VO_2 metasurface, several works expanded upon this design by extending the operating frequencies into the near- and mid-IR [250, 251] and increasing the ON/OFF extinction ratio by orders of magnitude [252]. Temperature-induced phase transitions were still the predominant method of control; however, in 2012, the first all-optical modulated VO_2 metasurface was demonstrated using the large field enhancement in SRR gaps and picosecond THz pulses (Figure 8B) [245]. The IMT was attributed to generation Poole-Frenkel excitations via the extremely high electric fields within the VO_2 layer. In addition to optical tuning, voltage switching of a VO_2 metasurface was also accomplished by using ionic gels covering a VO_2 + SRR metasurface [253]. In 2016, it was shown that the IMT temperature of VO_2 could be selectively and locally controlled via ion beam irradiation (Figure 8C) [246].

The second class of materials that have generated a considerable degree of excitement for tunable metasurface devices is GST. Unlike VO_2, GST is a phase change material (i.e. nonvolatile), which exhibits a stable crystalline-to-amorphous phase change for temperatures above the melting point (~600 K) and an amorphous-to-crystalline change for temperatures above the crystallization temperature (~160 K). Each phase will persist until an external source – electric, optical, thermal – "resets" the material; in this way, GST is a natural memory material and does not rely on hysteresis

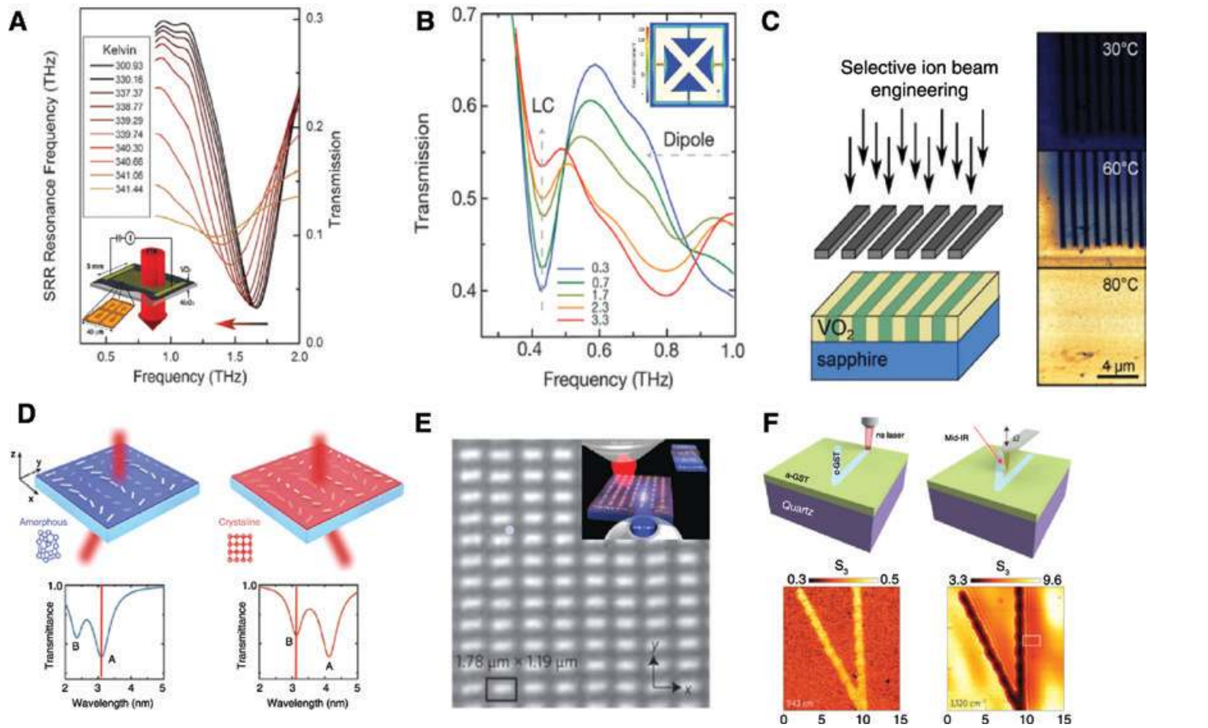

Figure 8: Phase-transition materials for metasurface applications.
(A) Memory metasurface consisting of gold SRR on VO_2 films. Electronic contacts provide heat to raise the temperature of the VO_2 layer and induced a memory capacitance via a hysteretic phase transition. For larger temperatures, the resonance of the device (see inset) is red-shifted. (B) Ultrafast modulation of SRR on VO_2 substrate with terahertz electric fields. The large electric fields in the SRR gaps induce an insulator-metal transition in the underlying VO_2 substrate and actively shift the resonance of the metasurface (see inset). (C) VO_2 films selectively irradiated using ion beams to alter the local defect concentrations; consequentially, the irradiated areas exhibit a much lower insulator-to-metal phase transitions temperature, and the film will exhibit a subwavelength variation in refractive index when heated. By judiciously controlling the ion pattern, intrinsic metasurfaces, such as waveplates, can be designed. (D) Schematic of an active metasurface utilizing GST for dynamic beam steering. Switching between the amorphous (red) and crystalline (blue) phase of the underlying GST layer dynamically switches the resonance of the metasurface from resonance A to resonance B and changes the direction of the transmitted beam. (E) Reconfigurable photonic metasurface using a thin film of GST sandwiched between ZnS-SiO_2 and a femtosecond laser source for writing. The top image shows the reflection map of the dielectric metasurface written into the GST film. The bottom image shows the transmission and reflection for horizontally polarized light. (F) V-shaped antenna wrote into a 30-nm-thick amorphous GST layer using a nanosecond laser and measured using near-IR nanoscopy. The bottom left and the right images show the dielectric contrast of the GST after being written and the generation of surface phonon-polaritons, respectively. (A) Reprinted with permission from [244], copyright 2009 by the American Association for the Advancement of Science; (B) reprinted with permission from [245], copyright 2012 by Springer Nature; (C) reprinted with permission from [246], copyright 2015 by the American Chemical Society; (D) reprinted from [247] under the Creative Commons (Attribution-Noncommercial) license; (E) reprinted with permission from [248], copyright 2015 by Springer Nature; (F) reprinted with permission from [249], copyright 2017 by Springer Nature.

effects like VO_2. The amorphous and crystalline phases have excellent optical contrast throughout the IR wavelengths, which make them ideal as a tunable material platform for MMs.

GST's potential as a memory material has been known since the 1980s, when it was first considered for energy storage devices; however, it was not until three decades later that the first GST MM was demonstrated. In 2013, Gholipour et al. designed and fabricated a multilayer metasurface composed of a sandwiched GST film between two buffer layers of ZnS/SiO_2 on top of a gold metasurface. By switching from amorphous-to-crystalline states using a 660-nm short- and high-intensity pulse and crystalline-to-amorphous states using a longer and lower-intensity pulse, the authors were able to switch the resonance of the metasurface antennas and modulate the near- and mid-IR reflection by as much as 400% (Figure 8D) [254]. The metasurface was able to endure 50 amorphous-to-crystalline cycles before showing degradation. In the same year, Chen et al. [255] patterned gold nanodisks directly on a 20-nm-thick GST layer and demonstrated nonvolatile tuning across a 1.89–2.27 µm range via thermal heating. In addition to metallic metasurface designs, GST has been incorporated in all-dielectric metasurfaces for functional tuning at visible and near-IR wavelengths [256]. Here, Karvounis et al. patterned sub-wavelength-thick GST films into a grating metasurface and demonstrated switching contrast ratios of 7 dB via a 532 nm laser excitation.

The application of the high-contrast change in optical properties of GST was efficiently utilized in the mid-IR spectrum, where losses are exceptionally low, by Michel et al. who demonstrated effective tuning of aluminum nanoantennas directly fabricated on GST. Here, the authors operated at 3000 cm^{-1}, where the relative change in the real portion of permittivity (ε_1) between amorphous (a) and crystalline states (c) was $\Delta\varepsilon_{1a\to c} = 27.2$, which corresponded with an antenna resonance shift of nearly 20% [257]. Tittl et al. [258] used a similar strategy for controlling a metal antenna metasurface but instead used GST as a spacer layer between an aluminum backing layer and an array of aluminum square antennas. Their design performed as a temperature-dependent switchable plasmonic perfect absorber from 3 to 5 μm with multispectral thermal imaging capabilities. Just recently in 2015, the same group demonstrated a tunable and switchable chiral metasurface with a mid-IR circular dichroism response from 4.15–4.90 μm [259]. Furthermore, by applying a bias layer to their design, the authors were able to flip the circular dichroism signal's sign using the large tunability of GST.

Of GST's remarkable optical properties, the ability to locally control the phase of the material is perhaps its most novel. In 2015, Wang et al. [248] demonstrated an all-optical reconfigurable dielectric metasurface based on a 70-nm-thick layer of GST sandwiched between ZnS/SiO_2 layers capable of generating nearly arbitrary reflection and transmission responses at near-IR frequencies. The metasurface was "written" using a femtosecond laser for generating the amorphous-to-crystalline phase change, a spatial light modulator for controlling the laser intensity pattern, and a microscope to focus this pattern down onto the GST layer (Figure 8E). In addition to a metasurface, a number of other planar optical components were demonstrated, including a visible bichromatic, multifocal Fresnel lens, a greyscale hologram, and a super-oscillatory lens. A similar and promising approach for generating mid-IR reconfigurable metasurfaces was recently demonstrated using crystalline GST as a phonon-polariton material [249]. Here, it was shown that micron-sized patterns of crystalline GST could be written using a nanosecond 660 nm laser and erased using the same laser, albeit with a longer pulse duration. The crystalline GST patterns could then support highly confined surface phonon-polariton modes (Figure 8F).

The impressive tunablility of GST and VO_2 has driven the exploration and discovery of other phase change/transition materials. Recently, a class of phase change materials within the perovskite family has emerged as promising alternative materials for tunable meta-devices. Strongly correlated samarium nickelate ($SmNiO_3$) is known to exhibit metal-insulator phase transitions at temperatures of approximately 140°C, similar to VO_2 and GST [260]. However, $SmNiO_3$ exhibits a second phase transition via electron doping, which can drastically change the optical properties of the film across a vast spectral range (0.4–17 μm). The electron doping effectively increases the bandgap of $SmNiO_3$ and is accomplished through either gas phase, liquid phase, or solid-state dopant injection. Li et al. [261] utilized this remarkably broadband tuning in their demonstration of several platinum on $SmNiO_3$ plasmonic metasurface structures using a variety of control inputs, including lithium intercalation, thermal annealing, and electrical biasing. Their finding suggests that $SmNiO_3$ is an ideal candidate for modulating absorption at mid-IR frequencies and holds great promise for thermal applications.

As a closing remark, it should be noted that there exists another class of materials that exhibit a metal-to-insulator phase change when subjected to gaseous chemical reagents, namely hydrogen. Since the conceptual emergence of hydrogen as an energy source, a large body of research has concentrated on effectively storing and sensing hydrogen gas. Palladium is well known to absorb substantial concentrations of hydrogen within its atomic lattice and sequentially transition into the dielectric phase known as palladium hydride; the phase transition is fully reversible upon removal of the hydrogen environment [262]. Additionally, palladium exhibits an LSP resonance throughout the ultraviolet, visible, and near-IR spectrum [263, 264]. These qualities have made palladium an attractive option for tunable metasurface devices, particularly ones that are functionalized for hydrogen sensing applications. In 2011, Tittl et al. [265] demonstrated a perfect absorbing metasurface structure composed of palladium strips optimized to detect changes in hydrogen concentrations as low as 0.5% in a matter of seconds. Similar hydrogen-induced phase transitions have been observed in other metals, such as yttrium and magnesium [266–268].

5 Outlook

The proliferation of new and promising materials for both metal- and dielectric-based metasurfaces has invigorated researchers to pursue metasurface physics and applications that were before impractical and/or impossible with conventional materials.

Recently, a growing interest to incorporate both spatial- and time-varying gradients across an interface has driven the pursuit of spatiotemporal metasurfaces. In conventional metasurface designs, additional momentum is provided to incoming light via the spatial phase-gradient of the nanoresonators. With the advent of ultrafast and highly nonlinear materials such as graphene and MOs, it may now be possible to additionally add a temporal phase gradient by switching the optical properties of individual resonators in a sequential order. The time-varying gradient will then impart additional energy to incoming light, thereby providing a Doppler-like shift in the frequency. Shaltout et al. [269] has shown that a spatiotemporal metasurface would lead to a generalized version of Snell's law, where both momentum and energy constraints are relaxed and several pertinent applications could be realized, such as nonreciprocal mirrors, magnetic-free isolators, and ultrafast beam steering. Hadad et al. [270] have theoretically realized a spatiotemporal metasurface with a nonreciprocal electromagnetic induced transparency window. However, to date, experimental realization of a time-varying metasurface has yet to be achieved. One possible strategy for realizing the selective switching capability is to utilize the ultrafast modulation capabilities of MOs and spatial and temporal shaped pump pulses.

Another avenue of prospective research is bringing metasurfaces into subnanometer dimensions. Conventional metasurface antennas are typically several nanometers thick – hundreds of nanometers for dielectric antennas – but the emergence of single or few monolayer thick plasmonic materials has opened an exciting opportunity to study light-matter interactions at these tiny dimensions. As shown in the pioneering work of Rivera et al. [271] plasmons confined to a single layer are capable of transitions that are "forbidden" in bulk materials and exhibit unique phenomena such as high-order multiple transitions, two-plasmon spontaneous emission, and singlet-triplet phosphorescence. As such, it may be possible to design metasurface devices capable of achieving these effects where the metasurface antennas are composed of 2D or monolayer materials such as graphene or the recently emerging MXenes. Besides naturally occurring 2D materials, there is a keen interest to bring crystalline metals, such as silver and TiN, to monolayer thicknesses. The advantage of this approach would be the high carrier concentrations within these noble metals, which would bring the applications wavelength closer to near-IR and visible wavelengths.

In summary, we have reviewed contemporary research in the development of novel material platforms for metasurface devices and applications. Although we have covered a wide range of emerging materials, we acknowledge that there are many material candidates for metasurfaces and many more to be discovered every year. We foresee optical metasurfaces as being exceptional devices for controlling the flow of light and a technology that will advance modern photonic technologies.

Acknowledgement: Air Force Office of Scientific Research (AFOSR) awards FA9550-14-1-0389 and FA9550-18-1-0002 and the U.S. Department of Energy, Office of Basic Energy Sciences, Division of Materials Sciences and Engineering under Award DE-SC0017717 (C.D. support). A.V.K. acknowledges support from DARPA/DSO Extreme Optics and Imaging (EXTREME) Program, Award HR00111720032.

References

[1] Shelby RA, Smith DR, Schultz S. Experimental verification of a negative index of refraction. Science 2001;292:77–9.
[2] Pendry JB. Negative refraction makes a perfect lens. Phys Rev Lett 2000;85:3966–9.
[3] Schurig D, Mock JJ, Justice BJ, et al. Metamaterial electromagnetic cloak at microwave frequencies. Science 2006;314:977–80.
[4] Holloway CL, Kuester EF, Gordon JA, O'Hara J, Booth J, Smith DR. An overview of the theory and applications of metasurfaces: the two-dimensional equivalents of metamaterials. IEEE Antennas Propag Mag 2012;54:10–35.
[5] Kildishev V, Boltasseva A, Shalaev VM. Planar photonics with metasurfaces. Science 2013;339:1232009.
[6] Yu N, Genevet P, Aieta F, et al. Flat optics: controlling wavefronts with optical antenna metasurfaces. IEEE J Sel Top Quantum Electron 2013;19:4700423.
[7] Yu N, Capasso F. Flat optics with designer metasurfaces. Nat Mater 2014;13:139–50.
[8] Walia S, Shah CM, Gutruf P, et al. Flexible metasurfaces and metamaterials: a review of materials and fabrication processes at micro- and nano-scales. Appl Phys Rev 2015;2:11303.
[9] Minovich AE, Miroshnichenko AE, Bykov AY, Murzina TV, Neshev DN, Kivshar YS. Functional and nonlinear optical metasurfaces. Laser Photon Rev 2015;205:9195–213.
[10] Genevet P, Capasso F. Holographic optical metasurfaces: a review of current progress. Rep Prog Phys 2015;78:24401.
[11] Chen H-T, Taylor AJ, Yu N. A review of metasurfaces: physics and applications. Rep Prog Phys 2016;79:76401.
[12] Hsiao H-H, Chu CH, Tsai DP. Fundamentals and applications of metasurfaces. Small Methods 2017;1:1600064.
[13] Meinzer N, Barnes WL, Hooper IR. Plasmonic meta-atoms and metasurfaces. Nat Photonics 2014;8:889–98.
[14] Glybovski SB, Tretyakov SA, Belov PA, Kivshar YS, Simovski CR. Metasurfaces: from microwaves to visible. Physics Rep 2016;634:1–72.

[15] Zhu AY, Kuznetsov AI, Luk'yanchuk B, Engheta N, Genevet P. Traditional and emerging materials for optical metasurfaces. Nanophotonics 2017;6:452–71.
[16] Colomban P. The use of metal nanoparticles to produce yellow, red and iridescent colour, from bronze age to present times in lustre pottery and glass: solid state chemistry, spectroscopy and nanostructure. J Nano Res 2009;8:109–32.
[17] Colomban P, Truong C. Non-destructive Raman study of the glazing technique in lustre potteries and faience (9–14th centuries): silver ions, nanoclusters, microstructure and processing. J Raman Spectrosc 2004;35:195–207.
[18] Hunt LB. Gold based glass and enamel colours. Endeavour 1981;5:61–7.
[19] Yu N, Genevet P, Kats MA, et al. Light propagation with phase discontinuities: generalized laws of reflection and refraction. Science 2011;334:333–7.
[20] Yin X, Ye Z, Rho J, Wang Y, Zhang X. Photonic spin Hall effect at metasurfaces. Science 2013;339:1405–7.
[21] Knight MW, Liu L, Wang Y, et al. Aluminum plasmonic nanoantennas. Nano Lett 2012;12:6000–4.
[22] Xu T, Du C, Wang C, Luo X. Subwavelength imaging by metallic slab lens with nanoslits. Appl Phys Lett 2007;91:201501.
[23] Srituravanich W, Pan L, Wang Y, Sun C, Bogy DB, Zhang X. Flying plasmonic lens in the near field for high-speed nanolithography. Nat Nanotechnol 2008;3:733–7.
[24] Ni X, Ishii S, Kildishev AV, Shalaev VM. Ultra-thin, planar, Babinet-inverted plasmonic metalenses. Light Sci Appl 2013;2:e72.
[25] Chen X, Huang L, Mühlenbernd H, et al. Dual-polarity plasmonic metalens for visible light. Nat Commun 2012;3:1198.
[26] Aieta F, Genevet P, Kats MA, et al. Aberration-free ultrathin flat lenses and axicons at telecom wavelengths based on plasmonic metasurfaces. Nano Lett 2012;12:4932–6.
[27] Khorasaninejad M, Chen WT, Devlin RC, Oh J, Zhu AY, Capasso F. Metalenses at visible wavelengths: diffraction-limited focusing and subwavelength resolution imaging. Science 2016;352:1190–4.
[28] Li Z, Palacios E, Butun S, Aydin K. Visible-frequency metasurfaces for broadband anomalous reflection and high-efficiency spectrum splitting. Nano Lett 2015;15:1615–21.
[29] Ni X, Kildishev AV, Shalaev VM. Metasurface holograms for visible light. Nat Commun 2013;4:2807.
[30] Zhou F, Liu Y, Cai W. Plasmonic holographic imaging with V-shaped nanoantenna array. Opt Express 2013;21:4348.
[31] Montelongo Y, Tenorio-Pearl JO, Milne WI, Wilkinson TD. Polarization switchable diffraction based on subwavelength plasmonic nanoantennas. Nano Lett 2014;14:294–8.
[32] Huang L, Chen X, Mühlenbernd H, et al. Three-dimensional optical holography using a plasmonic metasurface. Nat Commun 2013;4:2808.
[33] Zheng G, Mühlenbernd H, Kenney M, Li G, Zentgraf T, Zhang S. Metasurface holograms reaching 80% efficiency. Nat Nanotechnol 2015;10:308–12.
[34] Wen D, Yue F, Li G, et al. Helicity multiplexed broadband metasurface holograms. Nat Commun 2015;6:8241.
[35] Chen WT, Yang KY, Wang CM, et al. High-efficiency broadband meta-hologram with polarization-controlled dual images. Nano Lett 2014;14:225–30.
[36] Ye W, Zeuner F, Li X, et al. Spin and wavelength multiplexed nonlinear metasurface holography. Nat Commun 2016;7:11930.
[37] Montelongo Y, Tenorio-Pearl JO, Williams C, Zhang S, Milne WI, Wilkinson TD. Plasmonic nanoparticle scattering for color holograms. Proc Natl Acad Sci USA 2014;7:1–5.
[38] Huang Y-W, Chen WT, Tsai W-Y, et al. Aluminum plasmonic multicolor meta-Hologram. Nano Lett 2015;15:3122–7.
[39] Li X, Chen L, Li Y, et al. Multicolor 3D meta-holography by broadband plasmonic modulation. Sci Adv 2016;2:e1601102.
[40] Choudhury S, Guler U, Shaltout A, Shalaev VM, Kildishev AV, Boltasseva A. Pancharatnam-berry phase manipulating metasurface for visible color hologram based on low loss silver thin film. Adv Opt Mater 2017;5:1700196.
[41] Zhao Y, Alù A. Manipulating light polarization with ultrathin plasmonic metasurfaces. Phys Rev B 2011;84:205428.
[42] Bomzon Z, Biener G, Kleiner V, Hasman E. Space-variant Pancharatnam-Berry phase optical elements with computer-generated subwavelength gratings. Opt Lett 2002;27:1141.
[43] Yu N, Aieta F, Genevet P, Kats MA, Gaburro Z, Capasso F. A broadband, background-free quarter-wave plate based on plasmonic metasurfaces. Nano Lett 2012;12:6328–33.
[44] Karimi E, Schulz SA, De Leon I, Qassim H, Upham J, Boyd RW. Generating optical orbital angular momentum at visible wavelengths using a plasmonic metasurface. Light Sci Appl 2014;3:e167.
[45] Ding F, Wang Z, He S, Shalaev VM, Kildishev AV. Broadband high-efficiency half-wave plate: a supercell-based plasmonic metasurface approach. ACS Nano 2015;9:4111–9.
[46] Pors A, Bozhevolnyi SI. Efficient and broadband quarter-wave plates by gap-plasmon resonators. Opt Express 2013;21:2942.
[47] Yue F, Wen D, Xin J, Gerardot BD, Li J, Chen X. Vector vortex beam generation with a single plasmonic metasurface. ACS Photonics 2016;3:1558–63.
[48] Wang W, Li Y, Guo Z, et al. Ultra-thin optical vortex phase plate based on the metasurface and the angular momentum transformation. J Opt 2015;17:45102.
[49] Genevet P, Yu N, Aieta F, et al. Ultra-thin plasmonic optical vortex plate based on phase discontinuities. Appl Phys Lett 2012;100:13101.
[50] Ni X, Wong ZJ, Mrejen M, Wang Y, Zhang X. An ultrathin invisibility skin cloak for visible light. Science 2015;349:1310–4.
[51] Kim J, Choudhury S, DeVault C, et al. Controlling the polarization state of light with plasmonic metal oxide metasurface. ACS Nano 2016;10:9326–33.
[52] Ishii S, Kildishev AV, Shalaev VM, Chen K-P, Drachev VP. Metal nanoslit lenses with polarization-selective design: erratum. Opt Lett 2011;36:1244.
[53] Yang Y, Wang W, Moitra P, Kravchenko II, Briggs DP, Valentine J. Dielectric meta-reflect array for broadband linear polarization conversion and optical vortex generation. Nano Lett 2014;14:1394–9.
[54] Shaltout A, Liu J, Kildishev A, Shalaev V. Photonic spin Hall effect in gap–plasmon metasurfaces for on-chip chiroptical spectroscopy. Optica 2015;2:860.
[55] Khurgin JB. How to deal with the loss in plasmonics and metamaterials. Nat Nano 2015;10:2–6.
[56] Asadchy VS, Wickberg A, Díaz-Rubio A, Wegener M. Eliminating scattering loss in anomalously reflecting optical metasurfaces. ACS Photonics 2017;4:1264–70.
[57] Yokogawa S, Burgos SP, Atwater HA. Plasmonic color filters for CMOS image sensor applications. Nano Lett 2012;12:4349–54.

[58] Clausen JS, Højlund-Nielsen E, Christiansen AB, et al. Plasmonic metasurfaces for coloration of plastic consumer products. Nano Lett 2014;14:4499–504.
[59] Roberts AS, Pors A, Albrektsen O, Bozhevolnyi SI. Subwavelength plasmonic color printing protected for ambient use. Nano Lett 2014;14:783–7.
[60] Kruk S, Weismann M, Bykov AY, et al. Enhanced magnetic second-harmonic generation from resonant metasurfaces. ACS Photonics 2015;2:1007–12.
[61] Mamonov E, Kolmychek I, Maydykovsky A, Murzina T. Second harmonic generation in planar chiral nanostructures. Bull Russ Acad Sci 2013;77:66–8.
[62] Chandrasekar R, Emani NK, Lagutchev A, et al. Second harmonic generation with plasmonic metasurfaces: direct comparison of electric and magnetic resonances. Opt Mater Express 2015;5:2682.
[63] Gomez-Diaz JS, Lee J, Tymchenko M, Belkin MA, Alù A. Giant nonlinear processes in plasmonic metasurfaces. In: IEEE International Symposium on Antennas and Propagation & USNC/URSI National Radio Science Meeting 2015;2015:1084–5.
[64] Tymchenko M, Gomez-Diaz JS, Lee J, Nookala N, Belkin MA, Alù A, Gradient nonlinear Pancharatnam-Berry metasurfaces. Phys Rev Lett 2015;115:207403.
[65] Panchenko E, Cadusch JJ, James TD, Roberts A. Plasmonic metasurface-enabled differential photodetectors for broadband optical polarization characterization. ACS Photonics 2016;3:1833–9.
[66] Fang J, Wang D, DeVault CT, et al. Enhanced graphene photodetector with fractal metasurface. Nano Lett 2017;17:57–62.
[67] Maksymov IS. Magneto-plasmonic nanoantennas: basics and applications. Rev Phys 2016;1:36–51.
[68] Luk TS, Campione S, Kim I, et al. Directional perfect absorption using deep subwavelength low-permittivity films. Phys Rev B – Condens Matter Mater Phys 2014;90:1–10.
[69] Ding F, Dai J, Chen Y, Zhu J, Jin Y, Bozhevolnyi SI. Broadband near-infrared metamaterial absorbers utilizing highly lossy metals. Sci Rep 2016;6:39445.
[70] Aydin K, Ferry VE, Briggs RM, Atwater HA. Broadband polarization-independent resonant light absorption using ultrathin plasmonic super absorbers. Nat Commun 2011;2:517.
[71] Jiang ZH, Yun S, Toor F, Werner DH, Mayer TS. Conformal dual-band near-perfectly absorbing mid-infrared metamaterial coating. ACS Nano 2011;5:4641–7.
[72] Argyropoulos C, Le KQ, Mattiucci N, D'Aguanno G, Alù A. Broadband absorbers and selective emitters based on plasmonic Brewster metasurfaces. Phys Rev B 2013;87:205112.
[73] Akselrod GM, Huang J, Hoang TB, et al. Large-area metasurface perfect absorbers from visible to near-infrared. Adv Mater 2015;27:8028–34.
[74] Ng C, Cadusch JJ, Dligatch S, et al. Hot carrier extraction with plasmonic broadband absorbers. ACS Nano 2016;10:4704–11.
[75] Guler U, Boltasseva A, Shalaev VM. Refractory plasmonics. Science 2014;344:263–4.
[76] Dionne JA, Baldi A, Baum B, et al. Localized fields, global impact: industrial applications of resonant plasmonic materials. MRS Bull 2015;40:1138–45.
[77] Albrecht G, Kaiser S, Giessen H, Hentschel M. Refractory plasmonics without refractory materials. Nano Lett 2017;17:6402–8.
[78] Albrecht G, Ubl M, Kaiser S, Giessen H, Hentschel M. Comprehensive study of plasmonic materials in the visible and near-infrared: linear, refractory, and nonlinear optical properties. ACS Photonics 2018;5:1058–67.
[79] West PR, Ishii S, Naik GV, Emani NK, Shalaev VM, Boltasseva A. Searching for better plasmonic materials. Laser Photonics Rev 2010;4:795–808.
[80] Naik GV, Shalaev VM, Boltasseva A. Alternative plasmonic materials: beyond gold and silver. Adv Mater 2013;25:3264–94.
[81] Ni X, Emani NK, Kildishev AV, Boltasseva A, Shalaev VM. Broadband light bending with plasmonic nanoantennas. Science 2012;335:427.
[82] Genevet P, Capasso F, Aieta F, Khorasaninejad M, Devlin R. Recent advances in planar optics: from plasmonic to dielectric metasurfaces. Optica 2017;4:139.
[83] Staude I, Schilling J. Metamaterial-inspired silicon nanophotonics. Nat Photonics 2017; 11:274–84.
[84] Jahani S, Jacob Z. All-dielectric metamaterials. Nat Nanotechnol 2016;11:23–36.
[85] Kuznetsov AI, Miroshnichenko AE, Brongersma ML, Kivshar YS, Luk'yanchuk B. Optically resonant dielectric nanostructures. Science 2016;354. pii: aag2472.
[86] Campione S, Liu S, Basilio LI, et al. Broken symmetry dielectric resonators for high quality factor fano metasurfaces. ACS Photonics 2016;3:2362–7.
[87] Yang Y, Kravchenko II, Briggs DP, Valentine J. All-dielectric metasurface analogue of electromagnetically induced transparency. Nat Commun 2014;5:5753.
[88] Hsu CW, Zhen B, Stone AD, Joannopoulos JD, Soljačić M. Bound states in the continuum. Nat Rev Mater 2016;1:16048.
[89] Moitra P, Slovick BA, Gang Yu Z, Krishnamurthy S, Valentine J. Experimental demonstration of a broadband all-dielectric metamaterial perfect reflector. Appl Phys Lett 2014;104:171102.
[90] Moitra P, Slovick BA, li W, et al. Large-scale all-dielectric metamaterial perfect reflectors. ACS Photonics 2015;2:692–8.
[91] Kerker M, Wang D-S, Giles CL. Electromagnetic scattering by magnetic spheres. J Opt Soc Am 1983;73:765.
[92] Shcherbakov MR, Neshev DN, Hopkins B, et al. Enhanced third-harmonic generation in silicon nanoparticles driven by magnetic response. Nano Lett 2014;14:6488–92.
[93] Yang Y, Wang W, Boulesbaa A, et al. Nonlinear fano-resonant dielectric metasurfaces. Nano Lett 2015;15:7388–93.
[94] Hausmann BJM, Bulu I, Venkataraman V, Deotare P, Lončar M. Diamond nonlinear photonics. Nat Photonics 2014;8:369–74.
[95] Sipahigil A, Evans RE, Sukachev DD, et al. An integrated diamond nanophotonics platform for quantum-optical networks. Science 2016;354:847–50.
[96] Choy JT, Hausmann BJM, Babinec TM, et al. Enhanced single-photon emission from a diamond-silver aperture. Nat Photonics 2011;5:738–43.
[97] Babinec TM, Hausmann BJM, Khan M, et al. A diamond nanowire single-photon source. Nat Nanotechnol 2010;5:195–9.
[98] Li L, Schröder T, Chen EH, et al. Coherent spin control of a nanocavity-enhanced qubit in diamond. Nat Commun 2015;6:6173.
[99] Clevenson H, Trusheim ME, Teale C, Schröder T, Braje D, Englund D. Broadband magnetometry and temperature sensing with a light-trapping diamond waveguide. Nat Phys 2015;11:393–7.

[100] Chen EH, Gaathon O, Trusheim ME, Englund D. Wide-field multispectral super-resolution imaging using spin-dependent fluorescence in nanodiamonds. Nano Lett 2013;13:2073–7.
[101] Grote RR, Huang T-Y, Mann SA, et al. Imaging a nitrogen-vacancy center with a diamond immersion metalens. 2017. arXiv:1711.00901.
[102] Lalanne P, Astilean S, Chavel P, Cambril E, Launois H. Blazed binary subwavelength gratings with efficiencies larger than those of conventional échelette gratings. Opt Lett 1998;23:1081.
[103] Lalanne P, Astilean S, Chavel P, Cambril E, Launois H. Design and fabrication of blazed binary diffractive elements with sampling periods smaller than the structural cutoff. J Opt Soc Am A 1999;16:1143.
[104] Lalanne P. Waveguiding in blazed-binary diffractive elements. J Opt Soc Am A 1999;16:2517.
[105] Decker M, Staude I, Falkner M, et al. High-efficiency dielectric huygens' surfaces. Adv Opt Mater 2015;3:813–20.
[106] Yu YF, Zhu AY, Paniagua-Domínguez R, Fu YH, Luk'yanchuk B, Kuznetsov AI. High-transmission dielectric metasurface with 2π phase control at visible wavelengths. Laser Photonics Rev 2015;9:412–8.
[107] Shalaev MI, Sun J, Tsukernik A, Pandey A, Nikolskiy K, Litchinitser NM. High-efficiency all-dielectric metasurfaces for ultracompact beam manipulation in transmission mode. Nano Lett 2015;15:6261–6.
[108] Chong KE, Staude I, James A, et al. Polarization-independent silicon metadevices for efficient optical wavefront control. Nano Lett 2015;15:5369–74.
[109] Chong KE, Wang L, Staude I, et al. Efficient polarization-insensitive complex wavefront control using huygens' metasurfaces based on dielectric resonant meta-atoms. ACS Photonics 2016;3:514–9.
[110] Khorasaninejad M, Zhu AY, Roques-Carmes C, et al. Polarization-insensitive metalenses at visible wavelengths. Nano Lett 2016;16:7229–34.
[111] Lin D, Fan P, Hasman E, Brongersma ML. Dielectric gradient metasurface optical elements. Science 2014;345:298–302.
[112] Khorasaninejad M, Ambrosio A, Kanhaiya P, Capasso F. Broadband and chiral binary dielectric meta-holograms. Sci Adv 2016;2:e1501258.
[113] Niv A, Biener G, Kleiner V, Hasman E. Manipulation of the Pancharatnam phase in vectorial vortices. Opt Express 2006;14:4208.
[114] Khorasaninejad M, Chen WT, Oh J, Capasso F. Super-dispersive off-axis meta-lenses for compact high resolution spectroscopy. Nano Lett 2016;16:3732–7.
[115] Bomzon Z, Kleiner V, Hasman E. Pancharatnam-Berry phase in space-variant polarization-state manipulations with subwavelength gratings. Opt Lett 2001;26:1424.
[116] Naik GV, Schroeder JL, Ni X, Kildishev AV, Sands TD, Boltasseva A. Titanium nitride as a plasmonic material for visible and near-infrared wavelengths. Opt Mater Express 2012;2:478.
[117] Li W, Guler U, Kinsey N, et al. Refractory plasmonics with titanium nitride: broadband. Adv Mater 2014;47:7959–65.
[118] Chirumamilla M, Chirumamilla A, Yang Y, et al. Large-area ultrabroadband absorber for solar thermophotovoltaics based on 3D titanium nitride nanopillars. Adv Opt Mater 2017;5:1700552.
[119] Guler U, Ndukaife JC, Naik GV, et al. Local heating with lithographically fabricated plasmonic titanium nitride nanoparticles. Nano Lett 2013;13:6078–83.
[120] Chaudhuri K, Shaltout A, Guler U, Shalaev VM, Boltasseva A. High efficiency phase gradient metasurface using refractory plasmonic zirconium nitride. In: Conference on Lasers and Electro-Optics 2016:FM3N.2. OSA Technical Digest (online). Washington, DC, USA, Optical Society of America, 2016.
[121] Hu J, Ren X, Reed AN, et al. Evolutionary design and prototyping of single crystalline titanium nitride lattice optics. ACS Photonics 2017;4:606–12.
[122] Gui L, Bagheri S, Strohfeldt N, et al. Nonlinear refractory plasmonics with titanium nitride nanoantennas. Nano Lett 2016;16:5708–13.
[123] Liu Y, Matsukawa T, Endo K, et al. Advanced FinFET CMOS technology: TiN-Gate, fin-height control and asymmetric gate insulator thickness 4T-FinFETs. In: International Electron Devices Meeting. Piscataway, NJ, USA, IEEE, 2006:1–4.
[124] Garcia AS, Diniz JA, Swart JW, Lima LPB, dos Santos MVP. Formation and characterization of tin layers for metal gate electrodes of CMOS capacitors. In: International Caribbean Conference on Devices, Circuits and Systems (ICCDCS) 2014:1–6.
[125] Bagheri S, Zgrabik CM, Gissibl T, et al. Large-area fabrication of TiN nanoantenna arrays for refractory plasmonics in the mid-infrared by femtosecond direct laser writing and interference lithography [Invited]. Opt Mater Express 2015;5:2625.
[126] Shah D, Reddy H, Kinsey N, Shalaev VM, Boltasseva A. Optical properties of plasmonic ultrathin TiN films. Adv Opt Mater 2017;5. https://doi.org/10.1364/CLEO_SI.2017.SM4K.3.
[127] Reddy H, Guler U, Kudyshev Z, Kildishev AV, Shalaev VM, Boltasseva A. Temperature-dependent optical properties of plasmonic titanium nitride thin films. ACS Photonics 2017;4:1413–20.
[128] Guler U, Suslov S, Kildishev AV, Boltasseva A, Shalaev VM. Colloidal plasmonic titanium nitride nanoparticles: properties and applications. Nanophotonics 2015;4:269–76.
[129] Guler U, Shalaev VM, Boltasseva A. Nanoparticle plasmonics: going practical with transition metal nitrides. Materials Today 2015;18:227–37.
[130] Naldoni A, Guler U, Wang Z, et al. Broadband hot-electron collection for solar water splitting with plasmonic titanium nitride. Adv Opt Mater 2017;5:1601031.
[131] Kinsey N, Syed AA, Courtwright D, et al. Effective third-order nonlinearities in metallic refractory titanium nitride thin films. Opt Mater Express 2015;5:2395.
[132] Capretti A, Wang Y, Engheta N, Dal Negro L. Comparative study of second-harmonic generation from epsilon-near-zero indium tin oxide and titanium nitride nanolayers excited in the near-infrared spectral range. ACS Photonics 2015;2:1584–91.
[133] Reichelt K, Lutz H. Hetero-epitaxial growth of vacuum evaporated silver and gold. J Cryst Growth 1971;10:103–7.
[134] Bialas H, Heneka K. Epitaxy of fcc metals on dielectric substrates. Vacuum 1994;45:79–87.
[135] Park JH, Ambwani P, Manno M, et al. Single-crystalline silver films for plasmonics. Adv Mater 2012;24:3988–92.
[136] Wu Y, Zhang C, Estakhri NM, et al. Intrinsic optical properties and enhanced plasmonic response of epitaxial silver. Adv Mater 2017;26:6106–10.
[137] Johnson PB, Christy RW. Optical constants of the noble metals. Phys Rev B 1972;6:4370–9.

[138] Lu Y-J, Kim J, Chen H-Y, et al. Plasmonic nanolaser using epitaxially grown silver film. Science 2012;337:450–3.
[139] High AA, Devlin RC, Dibos A, et al. Visible-frequency hyperbolic metasurface. Nature 2015;522:192–6.
[140] Liu Y, Zhang X. Metasurfaces for manipulating surface plasmons. 2013;103:141101.
[141] West PR, Stewart JL, Kildishev AV, et al. All-dielectric subwavelength metasurface focusing lens. Opt Express 2014;22:26212.
[142] Arbabi A, Horie Y, Bagheri M, Faraon A. Dielectric metasurfaces for complete control of phase and polarization with subwavelength spatial resolution and high transmission. Nat Nano 2015;10:937–43.
[143] Ohana D, Desiatov B, Mazurski N, Levy U. Dielectric metasurface as a platform for spatial mode conversion in nanoscale waveguides. Nano Lett 2016;16:7956–61.
[144] Kim SW, Yee KJ, Abashin M, Pang L, Fainman Y. Composite dielectric metasurfaces for phase control of vector field. Opt Lett 2015;40:2453.
[145] Zhou Z, Li J, Su R, et al. Efficient silicon metasurfaces for visible light. ACS Photonics 2017;4:544–51.
[146] Wu C, Arju N, Kelp G, et al. Spectrally selective chiral silicon metasurfaces based on infrared Fano resonances. Nat Commun 2014;5:Article number: 3892. doi:10.1038/ncomms4892.
[147] Li Z, Kim M-H, Wang C, et al. Controlling propagation and coupling of waveguide modes using phase-gradient metasurfaces. Nat Nanotechnol 2017;12:675–83.
[148] Liu H, Guo C, Vampa G, et al. Enhanced high-harmonic generation from an all-dielectric metasurface. 2017. arXiv:1710.04244.
[149] Zhan A, Colburn S, Trivedi R, Fryett TK, Dodson CM, Majumdar A. Low-contrast dielectric metasurface optics. ACS Photonics 2016;3:209–14.
[150] Park C-S, Shrestha VR, Yue W, et al. Structural color filters enabled by a dielectric metasurface incorporating hydrogenated amorphous silicon nanodisks. Sci Rep 2017;7:2556.
[151] Fan Z-B, Shao Z-K, Xie M-Y, et al. Silicon nitride metalenses for unpolarized high-NA visible imaging. 2017.
[152] Bar-David J, Mazurski N, Levy U. *In situ* planarization of huygens metasurfaces by nanoscale local oxidation of silicon. ACS Photonics 2017;4:2359–66.
[153] Lalanne P, Chavel P. Metalenses at visible wavelengths: past, present, perspectives. Laser Photon Rev 2017;11:1600295.
[154] Devlin RC, Khorasaninejad M, Chen WT, Oh J, Capasso F. Broadband high-efficiency dielectric metasurfaces for the visible spectrum. Proc Natl Acad Sci 2016;113:10473–8.
[155] Balthasar Mueller JP, Rubin NA, Devlin RC, Groever B, Capasso F. Metasurface polarization optics: independent phase control of arbitrary orthogonal states of polarization. Phys Rev Lett 2017;118:113901.
[156] Zhu AY, Chen W-T, Khorasaninejad M, et al. Ultra-compact visible chiral spectrometer with meta-lenses. APL Photonics 2017;2:36103.
[157] Chen WT, Zhu AY, Khorasaninejad M, Shi Z, Sanjeev V, Capasso F. Immersion meta-lenses at visible wavelengths for nanoscale imaging. Nano Lett 2017;17:3188–94.
[158] Khorasaninejad M, Chen WT, Zhu AY, et al. Multispectral chiral imaging with a metalens. Nano Lett 2016;16:4595–600.
[159] Devlin RC, Ambrosio A, Wintz D, et al. Spin-to-orbital angular momentum conversion in dielectric metasurfaces. Opt Express 2017;25:377.
[160] Gutruf P, Zou C, Withayachumnankul W, Bhaskaran M, Sriram S, Fumeaux C. Mechanically tunable dielectric resonator metasurfaces at visible frequencies. ACS Nano 2016; 10:133–41.
[161] Sun S, Zhou Z, Zhang C, et al. All-dielectric full-color printing with TiO2 metasurfaces. ACS Nano 2017; 11:4445–52.
[162] Adams DC, Inampudi S, Ribaudo T, et al. Funneling light through a subwavelength aperture with epsilon-near-zero materials. Phys Rev Lett 2011;107:133901.
[163] Gordon TR, Paik T, Klein DR, et al. Shape-dependent plasmonic response and directed self-assembly in a new semiconductor building block, indium-doped cadmium oxide (ICO). Nano Lett 2013;13:2857–63.
[164] Wang L, Clavero C, Yang K, et al. Bulk and surface plasmon polariton excitation in RuO_2 for low-loss plasmonic applications in NIR. Opt Express 2012;20:8618.
[165] Clerici M, Kinsey N, DeVault C, et al. Controlling hybrid nonlinearities in transparent conducting oxides via two-colour excitation. Nat Commun 2017;8:15829.
[166] Alam MZ, De Leon I, Boyd RW. Large optical nonlinearity of indium tin oxide in its epsilon-near-zero region. Science 2016;352:795–7.
[167] Park J, Kang JH, Kim SJ, Liu X, Brongersma ML. Dynamic reflection phase and polarization control in metasurfaces. Nano Lett 2017;17:407–13.
[168] Lee HW, Papadakis G, Burgos SP, et al. Nanoscale conducting oxide PlasMOStor. Nano Lett 2014;14:6463–8.
[169] Robusto PF, Braunstein R. Optical measurements of the surface plasmon of indium-tin oxide. Phys stat sol 1990;119;155–68.
[170] Gregory SA, Wang Y, De Groot CH, Muskens OL. Extreme subwavelength metal oxide direct and complementary metamaterials. ACS Photonics 2015;2:606–14.
[171] Guo P, Schaller RD, Ketterson JB, Chang RPH. Ultrafast switching of tunable infrared plasmons in indium tin oxide nanorod arrays with large absolute amplitude. Nat Photonics 2016; 10:267–73.
[172] Kim J, Naik GV, Emani NK, Guler U, Boltasseva A. Plasmonic resonances in nanostructured transparent conducting oxide films. IEEE J Sel Top Quantum Electron 2013;19:1–7.
[173] Kim J, Dutta A, Memarzadeh B, Kildishev AV, Mosallaei H, Boltasseva A. Zinc oxide based plasmonic multilayer resonator: localized and gap surface plasmon in the infrared. ACS Photonics 2015;2:1224–30.
[174] Abb M, Albella P, Aizpurua J, Muskens OL. All-optical control of a single plasmonic nanoantenna-ITO hybrid. Nano Lett 2011;11:2457–63.
[175] Abb M, Wang Y, de Groot CH, Muskens OL. Hotspot-mediated ultrafast nonlinear control of multifrequency plasmonic nanoantennas. Nat Commun 2016;5:4869.
[176] Metzger B, Hentschel M, Schumacher T, et al. Doubling the efficiency of third harmonic generation by positioning ITO nanocrystals into the hot-spot of plasmonic gap-antennas. Nano Lett 2014;14:2867–72.
[177] Tice DB, Li SQ, Tagliazucchi M, Buchholz DB, Weiss EA, Chang RPH. Ultrafast modulation of the plasma frequency of vertically aligned indium tin oxide rods. Nano Lett 2014;14:1120–6.
[178] Li S-Q, Guo P, Buchholz DB, et al. Plasmonic-photonic mode coupling in indium-tin-oxide nanorod arrays. ACS Photonics 2014;1:163–72.

[179] Guo P, Schaller RD, Ocola LE, Diroll BT, Ketterson JB, Chang RPH. Large optical nonlinearity of ITO nanorods for sub-picosecond all-optical modulation of the full-visible spectrum. Nat Commun 2016;7:12892.
[180] Guo P, Weimer MS,. Emery JD, et al. Conformal coating of a phase change material on ordered plasmonic nanorod arrays for broadband all-optical switching. ACS Nano 2017;11:693–701.
[181] Kinsey N, DeVault C, Kim J, Ferrera M, Shalaev VM, Boltasseva A. Epsilon-near-zero Al-doped ZnO for ultrafast switching at telecom wavelengths. Optica 2015;2:616.
[182] Alam MZ, Leon ID, Boyd RW. Large optical nonlinearity of indium tin oxide in its epsilon-near-zero region. Science 2016;352:795–7.
[183] Caspani L, Kaipurath RPM, Clerici M, et al. Enhanced nonlinear refractive index in ε-near-zero materials. Phys Rev Lett 2016;116:233901.
[184] Hoang TB, Mikkelsen MH. Broad electrical tuning of plasmonic nanoantennas at visible frequencies. Appl Phys Lett 2016;108:183107. https://doi.org/10.1063/1.4948588.
[185] Liu X, Kang J-H, Yuan H, et al. Electrical tuning of a quantum plasmonic resonance. Nat Nanotechnol 2017;12:866–70.
[186] Huang YW, Lee HWH, Sokhoyan R, et al. Gate-tunable conducting oxide metasurfaces. Nano Lett 2016;16:5319–25.
[187] Geim AK, Novoselov KS. The rise of graphene. Nat Mater 2007;6:183–91.
[188] Novoselov KS, Geim AK, Morozov SV, et al. Electric field effect in atomically thin carbon films. Science 2004; 306:666–9.
[189] Hwang EH, Das Sarma S. Dielectric function, screening, and plasmons in two-dimensional graphene. Phys Rev B – Condens Matter Mater Phys 2007;75:1–6.
[190] Jablan M, Buljan H, Soljačić M. Plasmonics in graphene at infrared frequencies. Phys Rev B 2009;80:245435.
[191] Koppens FHL, Chang DE, García de Abajo FJ. Graphene plasmonics: a platform for strong light-matter interactions. Nano Lett 2011;11:3370–7.
[192] García de Abajo FJ. Graphene plasmonics: challenges and opportunities. ACS Photonics 2014;1:135–52.
[193] Brar VW, Jang MS, Sherrott M, Lopez JJ, Atwater HA. Highly confined tunable mid-infrared plasmonics in graphene nanoresonators. Nano Lett 2013;13:2541–7.
[194] Rodrigo D, Limaj O, Janner D, et al. Mid-infrared plasmonic biosensing with graphene. Science 2015;349: 165–8.
[195] Fang Z, Thongrattanasiri S, Schlather A, et al. Gated tunability and hybridization of localized plasmons in nanostructured graphene. ACS Nano 2013;7:2388–95.
[196] Yao Y, Kats MA, Shankar R, et al. Wide wavelength tuning of optical antennas on graphene with nanosecond response time. Nano Lett 2014;14:214–9.
[197] Fei Z, Andreev GO, Bao W, et al. Infrared nanoscopy of dirac plasmons at the graphene-SiO2 interface. Nano Lett 2011;11:4701–5.
[198] Fei Z, Rodin AS, Andreev GO, et al. Gate-tuning of graphene plasmons revealed by infrared nano-imaging. Nature 2012;487:82–5.
[199] Chen J, Badioli M, Alonso-González P, et al. Optical nano-imaging of gate-tunable graphene plasmons. Nature 2012;3–7.
[200] Silveiro I, Ortega JMP, García de Abajo FJ. Plasmon wave function of graphene nanoribbons. New J Phys 2015;17:83013.
[201] Yu R, Cox JD, Saavedra JRM, Garcia de Abajo FJ. Analytical modeling of graphene plasmons. ACS Photonics 2017;4:3106–14.
[202] Emani NK, Wang D, Chung T-F, et al. Plasmon resonance in multilayer graphene nanoribbons. Laser Photon Rev 2015;9:650–5.
[203] Yan H, Low T, Zhu W, et al. Damping pathways of mid-infrared plasmons in graphene nanostructures. Nat Photonics 2013;7:394–9.
[204] Strait JH, Nene PS, Chan W-M, et al. Confined plasmons in graphene microstructures: experiments and theory. Phys Rev B 2013;87:241410.
[205] Christensen J, Manjavacas A, Thongrattanasiri S, Koppens FHL, García de Abajo FJ. Graphene plasmon waveguiding and hybridization in individual and paired nanoribbons. ACS Nano 2012;6:431–40.
[206] Low T, Avouris P. Graphene plasmonics for terahertz to mid-infrared applications. ACS Nano 2014;8:1086–101.
[207] Thongrattanasiri S, Koppens FHL, García de Abajo FJ. Complete optical absorption in periodically patterned graphene. Phys Rev Lett 2012;108. https://doi.org/10.1103/PhysRevLett.108.047401.
[208] Yu R, Manjavacas A, García de Abajo FJ. Ultrafast radiative heat transfer. Nat Commun 2017;8:2.
[209] Emani NK, Kildishev AV, Shalaev VM, Boltasseva A. Graphene: a dynamic platform for electrical control of plasmonic resonance. Nanophotonics 2015;4:214–23.
[210] Emani NK, Chung T-F, Ni X, Kildishev AV, Chen YP, Boltasseva A. Electrically tunable damping of plasmonic resonances with graphene. Nano Lett 2012;12:5202–6.
[211] Yao Y, Shankar R, Kats MA, et al. Electrically tunable metasurface perfect absorbers for ultrathin mid-infrared optical modulators. Nano Lett 2014;14:6526–32.
[212] Yao Y, Kats MA, Genevet P, et al. Broad electrical tuning of graphene-loaded plasmonic antennas. Nano Lett 2013;13:1257–64.
[213] Mousavi SH, Kholmanov I, Alici KB, et al. Inductive tuning of Fano-resonant metasurfaces using plasmonic response of graphene in the mid-infrared. Nano Lett 2013;13:1111–7.
[214] Dabidian N, Kholmanov I, Khanikaev AB, et al. Electrical switching of infrared light using graphene integration with plasmonic Fano resonant metasurfaces. ACS Photonics 2015;2:216–27.
[215] Emani NK, Chung T-F, Kildishev AV, Shalaev VM, Chen YP, Boltasseva A. Electrical modulation of fano resonance in plasmonic nanostructures using graphene. Nano Lett 2013;14: 78–82.
[216] Echtermeyer TJ, Britnell L, Jasnos PK, et al. Strong plasmonic enhancement of photovoltage in graphene. Nat Commun 2011;2:458.
[217] Yao Y, Shankar R, Rauter P, et al. High-responsivity mid-infrared graphene detectors with antenna-enhanced photocarrier generation and collection. Nano Lett 2014;14:3749–54.
[218] Liu Y, Cheng R, Liao L, et al. Plasmon resonance enhanced multicolour photodetection by graphene. Nat Commun 2011;2:579.
[219] Echtermeyer TJ, Milana S, Sassi U, et al. surface plasmon polariton graphene photodetectors. Nano Lett 2016;16: 8–20.
[220] Maiti R, Sinha TK, Mukherjee S, Adhikari B, Ray SK. Enhanced and selective photodetection using graphene-stabilized

hybrid plasmonic silver nanoparticles. Plasmonics 2016;11:1297–304.
[221] Freitag M, Low T, Zhu W, Yan H, Xia F, Avouris P. Photocurrent in graphene harnessed by tunable intrinsic plasmons. Nat Commun 2013;4:1951.
[222] Cai X, Sushkov AB, Jadidi MM, et al. Plasmon-enhanced terahertz photodetection in graphene. Nano Lett 2015;15:4295–302.
[223] Chakraborty S, Marshall OP, Folland TG, Kim Y-J, Grigorenko AN, Novoselov KS. Gain modulation by graphene plasmons in aperiodic lattice lasers. Science 2016;351:246–8.
[224] Jang MS, Brar VW, Sherrott MC, et al. Tunable large resonant absorption in a midinfrared graphene Salisbury screen. Phys Rev B 2014;90:165409.
[225] Kim S, Jang MS, Brar VW, Tolstova Y, Mauser KW, Atwater HA. Electronically tunable extraordinary optical transmission in graphene plasmonic ribbons coupled to subwavelength metallic slit arrays. Nat Commun 2016;7:12323.
[226] Ma Z, Tahersima MH, Amin R, Khan S, Sorger VJ. Sub-wavelength plasmonic graphene-based slot electro-optic modulator. In: Frontiers in Optics 2017, 2017:FM2A.3.
[227] Amin R, Ma Z, Maiti R, et al. Attojoule-efficient graphene optical modulators. 2018. arXiv:1801.05046.
[228] Ding Y, Guan X, Zhu X, et al. Efficient electro-optic modulation in low-loss graphene-plasmonic slot waveguides. Nanoscale 2017;9:15576–81.
[229] Wang Y, Ou JZ, Chrimes AF, et al. Plasmon resonances of highly doped two-dimensional MoS2. Nano Lett 2015;15:883–90.
[230] Correas-Serrano D, Gomez-Diaz JS, Melcon AA, Alù A. Black phosphorus plasmonics: anisotropic elliptical propagation and nonlocality-induced canalization. J Opt 2016;18:104006.
[231] Lam K-T, Guo J. Plasmonics in strained monolayer black phosphorus. J Appl Phys 2015;117:113105.
[232] Xie X, Kang J, Cao W. et al. Designing artificial 2D crystals with site and size controlled quantum dots. Sci Rep 2017;7:9965.
[233] Butun S, Palacios E, Cain JD, Liu Z, Dravid VP, Aydin K. Quantifying plasmon-enhanced light absorption in monolayer WS2 films. ACS Appl Mater Interfaces 2017;9:15044–51.
[234] Palacios E, Park S, Butun S, Lauhon L, Aydin K. Enhanced radiative emission from monolayer MoS2films using a single plasmonic dimer nanoantenna. Appl Phys Lett 2017;111. doi: 10.1063/1.4993427.
[235] Wu L, Guo J, Dai X, Xiang Y, Fan D. Sensitivity enhanced by MoS2-graphene hybrid structure in guided-wave surface plasmon resonance biosensor. Plasmonics 2017.
[236] Jiang L, Zeng S, Ouyang Q, et al. Graphene-TMDC-graphene hybrid plasmonic metasurface for enhanced biosensing: a theoretical analysis. Phys Status Solidi 2017;214:1700563.
[237] Liu Z, Aydin K. Localized surface plasmons in nanostructured monolayer black phosphorus. Nano Lett 2016;16:3457–62.
[238] Hassani Gangaraj SA, Low T, Nemilentsau A, Hanson GW. Directive surface plasmons on tunable two-dimensional hyperbolic metasurfaces and black phosphorus: Green's function and complex plane analysis. IEEE Trans. Antennas Propag 2017;65:1174–86.
[239] Chen H, Chen Y, Yin J, Zhang X, Guo T, Yan P. High-damage-resistant tungsten disulfide saturable absorber mirror for passively Q-switched fiber laser. Opt Express 2016;24:16287.
[240] Wang Z, Dong Z, Gu Y, et al. Giant photoluminescence enhancement in tungsten-diselenide-gold plasmonic hybrid structures. Nat Commun 2016;7:11283.
[241] Yang Z, Ko C, Ramanathan S. Oxide electronics utilizing ultrafast metal-insulator transitions. Annu Rev Mater Res 2011;41:337–67.
[242] Mott NF. Metal-insulator transition. Rev Mod Phys 1968;40:677–83.
[243] Driscoll T, Palit S, Qazilbash MM, et al. Dynamic tuning of an infrared hybrid-metamaterial resonance using vanadium dioxide. Appl Phys Lett 2008;93:24101.
[244] Driscoll T, Kim H-T, Chae B-G, et al. Memory metamaterials. Science 2009;325:1518–21.
[245] Liu M, Hwang HY, Tao H, et al. Terahertz-field-induced insulator-to-metal transition in vanadium dioxide metamaterial. Nature 2012;487:345–8.
[246] Rensberg J, Zhang S, Zhou Y, et al. Active optical metasurfaces based on defect-engineered phase-transition materials. Nano Lett 2016;16:1050–5.
[247] Yin X, Steinle T, Huang L, et al. Beam switching and bifocal zoom lensing using active plasmonic metasurfaces. Light Sci Appl 2017;6:e17016.
[248] Wang Q, Rogers ETF, Gholipour B, et al. Optically reconfigurable metasurfaces and photonic devices based on phase change materials. Nat Photonics 2015;10:60–5.
[249] Li P, Yang X, Maß TWW, et al. Reversible optical switching of highly confined phonon-polaritons with an ultrathin phase-change material. Nat Mater 2016;15:870–5.
[250] Dicken MJ, Aydin K, Pryce IM, et al. Frequency tunable near-infrared metamaterials based on VO2 phase transition. Opt Express 2009;17:18330–9.
[251] Kats MA, Blanchard O, Genevet P, et al. Thermal tuning of mid-infrared plasmonic antenna arrays using a phase change material. Opt Lett 2013;38:368–70.
[252] Seo M, Kyoung J, Park H, et al. Active terahertz nanoantennas based on VO2 phase transition. Nano Lett 2010;10:2064–8.
[253] Goldflam MD, Liu MK, Chapler BC, et al. Voltage switching of a VO2 memory metasurface using ionic gel. Appl Phys Lett 2014;105:041117.
[254] Gholipour B, Zhang J, MacDonald KF, Hewak DW, Zheludev NI. An all-optical, non-volatile, bidirectional, phase-change meta-switch. Adv Mater 2013;25:3050–4.
[255] Chen YG, Kao TS, Ng B, et al. Hybrid phase-change plasmonic crystals for active tuning of lattice resonances. Opt Express 2013; 21:13691.
[256] Karvounis A, Gholipour B, MacDonald KF, Zheludev NI. All-dielectric phase-change reconfigurable metasurface. Appl Phys Lett 2016;109:051103. https://doi.org/10.1063/1.49592724.
[257] Michel AKU, Chigrin DN, Maß TWW, et al. Using low-loss phase-change materials for mid-infrared antenna resonance tuning. Nano Lett 2013;13:3470–5.
[258] Tittl A, Michel A-KU, Schäferling M, et al. A switchable mid-infrared plasmonic perfect absorber with multispectral thermal imaging capability. Adv Mater 2015;27: 4597–603.
[259] Yin X, Schäferling M, Michel A-KU, et al. Active chiral plasmonics. Nano Lett 2015;15:4255–60.
[260] Shi J, Zhou Y, Ramanathan S. Colossal resistance switching and band gap modulation in a perovskite nickelate by electron doping. Nat Commun 2014;5:Article number: 4860. doi: 10.1038/ncomms5860.
[261] Li Z, Zhou Y, Qi H, et al. Correlated perovskites as a new platform for super-broadband-tunable photonics. Adv Mater 2016;28:9117–25.

[262] Liu N, Tang ML, Hentschel M, Giessen H, Alivisatos AP. Nanoantenna-enhanced gas sensing in a single tailored nanofocus. Nat Mater 2011;10:631–6.
[263] Langhammer C, Zorić I, Larsson EM, Kasemo B. Localized surface plasmons shed light on nanoscale metal hydrides. Adv Mater 2010;22:4628–33.
[264] Langhammer C, Zorić I, Kasemo B, Clemens BM. Hydrogen storage in Pd nanodisks characterized with a novel nanoplasmonic sensing scheme. Nano Lett 2007;7:3122–7.
[265] Tittl A, Mai P, Taubert R, Dregely D, Liu N, Giessen H. Palladium-based plasmonic perfect absorber in the visible wavelength range and its application to hydrogen sensing. Nano Lett 2011;11:4366–9.
[266] Duan X, Kamin S, Sterl F, Giessen H, Liu N. Hydrogen-regulated chiral nanoplasmonics. Nano Lett 2016;16:1462–6.
[267] Sterl F, Strohfeldt N, Walter R, Griessen R, Tittl A, Giessen H. Magnesium as novel material for active plasmonics in the visible wavelength range. Nano Lett 2015;15:7949–55.
[268] Strohfeldt N, Tittl A, Schäferling M, et al. Yttrium hydride nanoantennas for active plasmonics. Nano Lett 2014;14:1140–7.
[269] Shaltout A, Kildishev A, Shalaev V. Time-varying metasurfaces and Lorentz non-reciprocity. Opt Mater Express 2015;5:2459.
[270] Hadad Y, Sounas DL, Alu A. Space-time gradient metasurfaces. Phys Rev B 2015;92:100304(R).
[271] Rivera N, Kaminer I, Zhen B, Joannopoulos JD, Soljačić M. Shrinking light to allow forbidden transitions on the atomic scale. Science 2016;353:263–9.